Linear stability analysis of strongly coupled fluid–structure problems with the Arbitrary-Lagrangian–Eulerian method

Jean-Lou Pfister, Olivier Marquet, Marco Carini

Available online at www.sciencedirect.com
ScienceDirect
Comput. Methods Appl. Mech. Engrg. 355 (2019) 663–689
Computer methods in applied mechanics and engineering
www.elsevier.com/locate/cma

Linear stability analysis of strongly coupled fluid–structure problems with the Arbitrary-Lagrangian–Eulerian method

Jean-Lou Pfister, Olivier Marquet*, Marco Carini

ONERA – The French Aerospace Lab, 8 rue des Vertugadins, 92190 MEUDON, France

Received 5 March 2019; received in revised form 17 June 2019; accepted 17 June 2019
Available online 8 July 2019

Abstract

The stability analysis of elastic structures strongly coupled to incompressible viscous flows is investigated in this paper, based on a linearization of the governing equations formulated with the Arbitrary-Lagrangian–Eulerian method. The exact linearized formulation, previously derived to solve the unsteady non-linear equations with implicit temporal schemes, is used here to determine the physical linear stability of steady states. Once discretized with a standard finite-element method based on Lagrange elements, the leading eigenvalues/eigenmodes of the linearized operator are computed for three configurations representative for classical fluid–structure interaction instabilities: the vortex-induced vibrations of an elastic plate clamped to the rear of a rigid cylinder, the flutter instability of a flag immersed in a channel flow and the vortex shedding behind a three-dimensional plate bent by the steady flow. The results are in good agreement with instability thresholds reported in the literature and obtained with time-marching simulations, at a much lower computational cost. To further decrease this computational cost, the equations governing the solid perturbations are projected onto a reduced basis of free-vibration modes. This projection allows to eliminate the extension perturbation, a non-physical variable introduced in the ALE formalism to propagate the infinitesimal displacement of the fluid–solid interface into the fluid domain.

Keywords: Fluid–structure interaction; Linear stability analysis; Arbitrary-Lagrangian–Eulerian method

1. Introduction

In various industrial applications, the interaction of fluid flows with structures induces large deformations which can be detrimental in many cases, but also beneficial to the engineering system in other cases. For instance, flutter of airplanes wings or bridge decks results in premature fatigue and can even lead to fracture of the structure. The vortex-induced vibration of elongated marine risers is another example of an industrial system where structural oscillations are detrimental. On the contrary, energy harvesting devices are designed to exploit these vibrations and transform the mechanical energy into electricity. In both cases, being able to predict the onset of such oscillations allows a better design of the systems. This onset can be predicted numerically by simulating in time the deformation induced by the fluid–structure interaction, or by determining the linear stability of their steady equilibrium position, as proposed in this paper.

* Corresponding author.
E-mail address: olivier.marquet@onera.fr (O. Marquet).

https://doi.org/10.1016/j.cma.2019.06.024

In aeronautics, the linear stability of structures immersed in a fluid flow has a long history and often constitutes the first topic of classical books in aeroelasticity [1,2]. The threshold for static divergence and flutter instability of airplanes wings in cruise condition are usually predicted by the so-called flutter analysis, which relies on several hypotheses for modelling the structure, the fluid and their interaction. For instance, the spanwise deformation of the wing is often modelled by a spring-mounted two-dimensional airfoil section. The high Reynolds-number flow is considered as inviscid and irrotational, and thus described with potential equations. A quasi-steady approach is also used to couple the fluid and solid dynamics [3], since the characteristic time-scale for the flow (transit time of the fluid particles over the wing) is much smaller than the characteristic time-scale for the solid (wing vibration period). The effect of the flow onto the structural motion is then reduced to the computation of the so-called flutter derivatives. They are determined as the first-order coefficients of a Taylor expansion of the fluid loads with respect to the solid displacement and/or velocity variables. These coefficients appear in the structure equations as the so-called generalized aerodynamic forces [2] and allow to obtain a reduced model of the coupled fluid–structure dynamics. A linear stability analysis of this reduced model well predicts the critical flutter speed [4]. However, the flutter analysis is strictly valid only at the critical flutter speed [5], when the growth rate of the perturbation vanishes. Moreover, the domain of validity for this approach is difficult to extend, for instance when the fluid and solid time-scales separation does not hold, as in vortex-induced vibration problems for instance.

In the present paper, we follow a more general approach, known as the time-linearized approach [6] in aeroelasticity, which investigates the temporal evolution of small fluid–structure perturbations developing around steady solutions of the fully coupled fluid–structure equations. Unlike the flutter analysis previously described, the linearization of the governing equation is thus performed prior to any model reduction. A similar analysis, known as global stability analysis (see the reviews [7,8]) in hydrodynamics, is performed when considering the stability of flows developing around rigid structures. The equations governing the dynamics of infinitesimal flow perturbations developing around steady flows are determined by linearization of the Navier–Stokes equations written in a fixed spatial domain. In the context of fluid–structure interaction, an additional difficulty arises in the linearization process because of the Lagrangian motion of the fluid–solid interface.

In the early nineties, a substantial effort had been set on solving linearized flow equations coupled to an elastic solid model using the so-called *transpiration approach*, very popular in aeronautics. Derived from the work of Lightill [9] for simulating the changes in airfoil thickness, the infinitesimal motion of the fluid–solid interface is taken into account in the linearized equation *via* a simple modification of the velocity boundary condition applied at the equilibrium position of the fluid–solid interface. This *transpiration* velocity condition allows one to easily adapt a flow solver to treat the fluid–structure problem and to effectively perform unsteady aeroelastic simulations. The transpiration approach was first applied to inviscid flows [10–12], as for instance in the work by Fisher [12], who predicted flutter characteristics of an AGARD wing by coupling a modal solid dynamics solver to a compressible Euler solver. More recently, this transpiration approach was also extended to viscous turbulent flows, as in the work by Bekka [13] who performed aeroelastic computations of the nozzle of a rocket launcher engine using a Reynolds-Averaged Navier–Stokes solver coupled to a beam-element solid solver.

Although the transpiration approach (as derived in the early nineties) sounds quite attractive from a computational point of view, it entirely neglects an important physical effect, namely the coincidence of fluid and solid normal stresses at the interface. Indeed, a generic perturbation in the position of the fluid–solid interface does not only modify the velocity continuity condition but also the normal stress condition. A few exact derivations of linearized fluid–structure problems have therefore been achieved. There are basically two approaches for deriving the perturbative equation of a physical problem governed by a non-linear equation defined in a moving domain [14]. The perturbations are defined either in a fixed reference configuration (Lagrangian-based perturbations) or in the instantaneous, deformed configuration (Eulerian-based perturbations) [15]. These two approaches result eventually to two different descriptions of the *same* physical problem. Richter [16] and Richter and Wick [17] used for instance the Lagrangian-based approach to linearize the steady fluid–structure equations and then study in detail the associated adjoint equations, for the purpose of optimal control and error/parameter estimation. Considering a steady Stokes flow interacting with a string model, Van der Zee et al. [18] applied the two linearization approaches in order to derive the adjoint equations. In the formulation obtained for the Lagrangian-based perturbations, the coupling conditions at the fluid–solid interface are straightforward, but non-local couplings also exist in the fluid domain and result in significant modifications of the original equations. In the formulation obtained for the Eulerian-based perturbations, the linearized conservation equations are “simpler”, while the coupling conditions, localized

at the interface, are more complicated due to the presence of higher-order derivative terms. In the context of time-dependent fluid–structure problems, an Eulerian-based linearization was proposed by Fernandez & Le Tallec [19,20], based on the Arbitrary Lagrangian–Eulerian (ALE) formulation of the fluid–structure problem [21]. They found that in addition to the classical transpiration velocity, the linearized stress coupling results in an *added-stiffness* term that depends on higher-order derivatives of the steady fluid velocity and pressure, as well as on a deformation operator involving the derivatives of the interface displacement. However, the numerical examples proposed in the paper did not highlight the role of the added stiffness terms and the requirements needed for the proper and accurate capture of the second-order spatial derivatives. For these reasons, we rather follow the Lagrangian-based approach detailed hereafter, that results in a lower-order differential problem.

The Lagrangian-based approach was adopted in a discrete framework (finite-volume discretization) by Lesoinne et al. [5,22] to derive a linearized ALE formulation for inviscid compressible flows modelled with the Euler equations. The formulation is somehow extended in the present paper. First, the linearized formulation of the ALE equation is derived in a continuous framework, independently of the spatial discretization chosen. Secondly, viscous flows are considered and modelled with the incompressible Navier–Stokes equations. Similar linearized ALE formulations have been derived with the aim of simulating unsteady fluid–structure interaction problems with large-added mass effects [23,24]. Those unsteady simulations require indeed a fully implicit temporal discretization [25–28]. A non-linear system is solved at each time-step using a Newton method, and thus involves the linearized ALE equations around the solution computed at the previous iteration. The mathematical formulation proposed in the present paper is similar but the ALE formulation is linearized around the steady deformed configuration, both for the fluid and the solid domains. Moreover, the physical objective is to investigate the linear stability properties of the steady deformed solution, which requires an *exact* linearization at the continuous level [25], and then a consistent discretization of the resulting problem.

The paper is organized as follows. Section 2 first briefly introduces the non-linear ALE formulation for an elastic solid immersed in an incompressible viscous fluid. The continuous equations are then linearized about a steady solution based on a Lagrangian decomposition of the perturbations in the configuration corresponding to the steady deformed solution. The eigenvalue problem obtained after a modal decomposition of the perturbation is then presented, as well as the discretization based on finite-elements. Then, in Section 3 three fluid–structure configurations are studied more specifically: an elastic plate clamped on a rigid cylinder immersed in a viscous channel flow [29], a flag placed in a viscous channel flow [30] and a plate positioned perpendicular to an incoming flow [31]. The first configuration is representative of a vortex-induced-vibration instability, while the second accounts for a flutter-induced-vibration instability. The last case shows, in a three-dimensional setting, how static reconfiguration of a flexible obstacle affects the instabilities in the wake [32]. Obtained stability results are validated on these cases, and the specific features that come with our formulation are further assessed.

2. Governing equations for the stability analysis with the ALE method

We investigate here the motion of an elastic solid immersed in a Newtonian fluid. The fluid is characterized by its density ρ_{f}^* and its kinematic viscosity $\nu_{\mathrm{f}}^* = \eta_{\mathrm{f}}^*/\rho_{\mathrm{f}}^*$, where η_{f}^* is the dynamic viscosity. The superscript * is used in the following to indicate dimensional quantities. The fluid flow is characterized by a velocity scale U^* and the solid is characterized by a length scale L^*. It is assumed homogeneous of density ρ_{s}^*. Under the assumption of isotropy, its elasticity is defined with two parameters. The Young modulus E_{s}^* characterizes the stiffness while the Poisson coefficient ν_{s} evaluates the ratio between transverse and axial strains. The classical Lamé coefficients $\lambda_{\mathrm{s}}^* = E_{\mathrm{s}}^*\nu_{\mathrm{s}}/((1+\nu_{\mathrm{s}})(1-2\nu_{\mathrm{s}}))$ and $\mu_{\mathrm{s}}^* = E_{\mathrm{s}}^*/(2\,(1+\nu_{\mathrm{s}}))$ can also be used instead of the Young modulus and Poisson coefficient.

The reference velocity U^* and length L^*, specified later depending on the configuration investigated, are used in the following to make all of the fluid and solid variables non-dimensional, the reference time scale being L^*/U^*. The non-dimensional variables are then denoted without superscript *. The fluid–structure configurations investigated in the following are entirely characterized by four non-dimensional parameters:

$$\mathcal{R}_{\mathrm{e}} = U^*L^*/\nu_{\mathrm{f}}^* \quad , \quad \mathcal{M}_{\mathrm{s}} = \rho_{\mathrm{s}}^*/\rho_{\mathrm{f}}^* \quad , \quad E_s = E_{\mathrm{s}}^*/(\rho_{\mathrm{f}}^*U^{*2}) \quad \text{and} \quad \nu_{\mathrm{s}} \tag{1}$$

where the Reynolds number $\mathcal{R}_{\mathrm{e}}$ characterizes the fluid flow, the solid-to-fluid density ratio $\mathcal{M}_{\mathrm{s}}$ controls the strength of the inertia effects in the fluid–structure coupling, and the non-dimensional Young modulus E_s and Poisson coefficient ν_{s} characterize the solid elasticity. The last two non-dimensional parameters can be replaced by the non-dimensional Lamé coefficients $\lambda_{\mathrm{s}} = \lambda_{\mathrm{s}}^*/(\rho_{\mathrm{f}}^*U^{*2})$ and $\mu_{\mathrm{s}} = \mu_{\mathrm{s}}^*/(\rho_{\mathrm{f}}^*U^{*2})$.

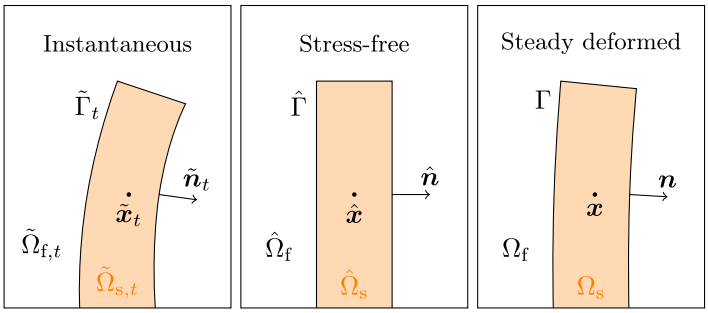

Fig. 1. Definitions of notations and spatial domains occupied by the fluid (white) and the solid (orange) in the instantaneous configuration (left), the stress-free reference configuration (middle) and the steady deformed reference configuration (right). Unlike in the instantaneous configuration, the fluid and solid domains are independent of time in the stress-free and steady configurations. (For interpretation of the references to colour in this figure legend, the reader is referred to the web version of this article.)

2.1. Non-linear ALE fluid–solid equations in the stress-free configuration

The motion of an elastic structure is classically defined in a Lagrangian framework. The position of any material point $\tilde{\boldsymbol{x}}_t$ in the instantaneous configuration (the spatial domain $\tilde{\Omega}_{\mathrm{s},t}$ occupied by the structure at time t shown in the left sketch of Fig. 1) is identified with respect to its position $\hat{\boldsymbol{x}}$ in an arbitrary reference configuration. A natural choice for this reference configuration is the stress-free configuration, i.e. the spatial domain $\hat{\Omega}_{\mathrm{s}}$ occupied by the structure when no external stresses are applied on it, as depicted in the sketch in the middle in Fig. 1. The solid displacement field $\hat{\boldsymbol{\xi}}_{\mathrm{s}}$ is then defined as the difference between the two positions:

$$\hat{\boldsymbol{\xi}}_{\mathrm{s}}(\hat{\boldsymbol{x}}, t) = \tilde{\boldsymbol{x}}_t - \hat{\boldsymbol{x}} \quad \text{for} \quad \hat{\boldsymbol{x}} \in \hat{\Omega}_{\mathrm{s}}. \tag{2}$$

The solid stresses are then expressed from the solid displacement by means of the first Piola–Kirchhoff stress tensor [33]

$$\hat{\mathbf{P}}(\hat{\boldsymbol{\xi}}_{\mathrm{s}}) = \hat{\mathbf{F}}(\hat{\boldsymbol{\xi}}_{\mathrm{s}})\,\hat{\mathbf{S}}(\hat{\boldsymbol{\xi}}_{\mathrm{s}}) \quad \text{with} \quad \hat{\mathbf{S}}(\hat{\boldsymbol{\xi}}_{\mathrm{s}}) = \lambda_{\mathrm{s}}\,\mathrm{tr}(\hat{\mathbf{E}}(\hat{\boldsymbol{\xi}}_{\mathrm{s}}))\mathbf{I} + 2\mu_{\mathrm{s}}\hat{\mathbf{E}}(\hat{\boldsymbol{\xi}}_{\mathrm{s}}), \tag{3}$$

where $\hat{\mathbf{F}}(\hat{\boldsymbol{\xi}}_{\mathrm{s}}) = \mathbf{I} + \hat{\boldsymbol{\nabla}}\hat{\boldsymbol{\xi}}_{\mathrm{s}}$ is the deformation gradient, $\hat{\mathbf{S}}$ is the second Piola–Kirchhoff stress tensor written here for a compressible Saint-Venant–Kirchhoff material, and

$$\hat{\mathbf{E}}(\hat{\boldsymbol{\xi}}_{\mathrm{s}}) = \frac{1}{2}\left(\hat{\mathbf{F}}(\hat{\boldsymbol{\xi}}_{\mathrm{s}})^{\mathrm{T}}\hat{\mathbf{F}}(\hat{\boldsymbol{\xi}}_{\mathrm{s}}) - \mathbf{I}\right). \tag{4}$$

is the Green–Lagrange strain tensor (where the superscript "T" denotes the transposition operator). Other types of strain–stress relations can be chosen, but are not considered here for the sake of simplicity. In the above equations, the notation $\hat{\boldsymbol{\nabla}} = \partial/\partial\hat{\boldsymbol{x}}$ refers to the differentiation operator with respect to the coordinates in the stress-free configuration.

On the other hand, the motion of an incompressible viscous fluid is classically defined in an Eulerian framework, with the Eulerian velocity and pressure fields $\tilde{\boldsymbol{u}}(\tilde{\boldsymbol{x}}_t, t)$ and $\tilde{p}(\tilde{\boldsymbol{x}}_t, t)$, for $\tilde{\boldsymbol{x}}_t \in \tilde{\Omega}_{\mathrm{f},t}$, satisfying the incompressible Navier–Stokes equations

$$\frac{\partial\tilde{\boldsymbol{u}}}{\partial t} + (\tilde{\boldsymbol{\nabla}}\tilde{\boldsymbol{u}})\tilde{\boldsymbol{u}} - \tilde{\boldsymbol{\nabla}}\cdot\tilde{\boldsymbol{\sigma}}(\tilde{\boldsymbol{u}}, \tilde{p}) = 0, \qquad \tilde{\boldsymbol{\nabla}}\cdot\tilde{\boldsymbol{u}} = 0 \qquad \text{in} \quad \tilde{\Omega}_{\mathrm{f},t}$$

where $\tilde{\boldsymbol{\sigma}}(\tilde{\boldsymbol{u}}, \tilde{p}) = -\tilde{p} + 1/\mathcal{R}_{\mathrm{e}}\,(\tilde{\boldsymbol{\nabla}}\tilde{\boldsymbol{u}} + \tilde{\boldsymbol{\nabla}}\tilde{\boldsymbol{u}}^{\mathrm{T}})$ is the fluid stress tensor written in the actual configuration, and $\tilde{\boldsymbol{\nabla}} = \partial/\partial\tilde{\boldsymbol{x}}_t$ denotes the differentiation with respect to the coordinates in the actual configuration. In the above formulation, both the velocity/pressure variables *and* the time-evolving domain are unknowns. The Arbitrary-Lagrangian–Eulerian (ALE) formalism [21,34] allows to rewrite the governing fluid equations in a *fixed* fluid domain $\hat{\Omega}_{\mathrm{f}}$ (for instance the stress-free reference configuration) while accounting explicitly for the deformation of the instantaneous fluid domain $\tilde{\Omega}_{\mathrm{f},t}$ induced by the solid deformation at the fluid–solid interface $\tilde{\Gamma}_t$ [34]. Like for the solid domain, the

deformation of the fluid domain is described in a Lagrangian framework by introducing an extension displacement field defined in the stress-free configuration as follows:

$$\hat{\boldsymbol{\xi}}_{\mathrm{e}}(\hat{\boldsymbol{x}}, t) = \tilde{\boldsymbol{x}}_t - \hat{\boldsymbol{x}} \quad \text{for} \quad \hat{\boldsymbol{x}} \in \hat{\Omega}_{\mathrm{f}}. \tag{5}$$

This non-physical variable is introduced in the ALE method so as to propagate the solid displacement at the fluid–structure interface $\hat{\Gamma}$ into the fluid domain, as

$$\mathbf{0} = \hat{\boldsymbol{\nabla}} \cdot \hat{\boldsymbol{\Sigma}}_{\mathrm{e}}(\hat{\boldsymbol{\xi}}_{\mathrm{e}}) \qquad \text{in} \quad \hat{\Omega}_{\mathrm{f}}, \tag{6}$$

$$\mathbf{0} = \hat{\boldsymbol{\xi}}_{\mathrm{e}} - \hat{\boldsymbol{\xi}}_{\mathrm{s}} \qquad \text{on} \quad \hat{\Gamma}, \tag{7}$$

where $\hat{\boldsymbol{\Sigma}}_{\mathrm{e}}$ is the so-called extension operator, often chosen in such a way that (6) is an elliptic equation, for instance the Laplace or a linear elasticity equation [35,36], in order to ensure a smooth propagation of the interface deformation. Enhanced models based on the biharmonic equation can also be used [37], but are not considered in the following. In the stress-free configuration, the fluid velocity and pressure fields are defined as $\hat{\boldsymbol{u}}(\hat{\boldsymbol{x}}, t) = \tilde{\boldsymbol{u}}(\tilde{\boldsymbol{x}}_t, t)$ and $\hat{p}(\hat{\boldsymbol{x}}, t) = \tilde{p}(\tilde{\boldsymbol{x}}_t, t)$ respectively. Compared to the usual form of the incompressible Navier–Stokes equation, additional terms are then found in the fluid equations due to the deformation of the fluid domain. A deformation operator $\hat{\boldsymbol{\Phi}}(\hat{\boldsymbol{\xi}}_{\mathrm{e}})$ is defined as a function of $\hat{\mathbf{F}}(\hat{\boldsymbol{\xi}}_{\mathrm{e}})$ the deformation gradient *in the fluid domain*, and $\hat{\mathrm{J}}(\hat{\boldsymbol{\xi}}_{\mathrm{e}})$ the transformation Jacobian, as

$$\hat{\boldsymbol{\Phi}}(\hat{\boldsymbol{\xi}}_{\mathrm{e}}) = \hat{\mathrm{J}}(\hat{\boldsymbol{\xi}}_{\mathrm{e}})\hat{\mathbf{F}}(\hat{\boldsymbol{\xi}}_{\mathrm{e}})^{-1}, \quad \hat{\mathbf{F}}(\hat{\boldsymbol{\xi}}_{\mathrm{e}}) = \mathbf{I} + \hat{\boldsymbol{\nabla}}\hat{\boldsymbol{\xi}}_{\mathrm{e}}, \quad \hat{\mathrm{J}}(\hat{\boldsymbol{\xi}}_{\mathrm{e}}) = \det(\hat{\mathbf{F}}(\hat{\boldsymbol{\xi}}_{\mathrm{e}})). \tag{8}$$

This deformation operator expresses how an infinitesimal surface in the instantaneous configuration is transformed in the reference configuration [38]. Note that in the two-dimensional case, $\hat{\boldsymbol{\Phi}}$ is an affine operator, while it is quadratic in the three-dimensional case. In the stress-free reference configuration, the first Piola–Kirchhoff stress tensor for the fluid finally writes as

$$\hat{\boldsymbol{\Sigma}}(\hat{\boldsymbol{u}}, \hat{p}, \hat{\boldsymbol{\xi}}_{\mathrm{e}}) = \hat{\boldsymbol{\sigma}}(\hat{\boldsymbol{u}}, \hat{p}, \hat{\boldsymbol{\xi}}_{\mathrm{e}})\, \hat{\boldsymbol{\Phi}}(\hat{\boldsymbol{\xi}}_{\mathrm{e}})^{\mathrm{T}}, \tag{9}$$

where $\hat{\boldsymbol{\sigma}}$ is the Cauchy stress tensor recasted in the stress-free configuration,

$$\hat{\boldsymbol{\sigma}}(\hat{\boldsymbol{u}}, \hat{p}, \hat{\boldsymbol{\xi}}_{\mathrm{e}}) = -\hat{p}\,\mathbf{I} + \frac{1}{\mathcal{R}_{\mathrm{e}}} \frac{1}{\hat{\mathrm{J}}(\hat{\boldsymbol{\xi}}_{\mathrm{e}})} \left((\hat{\boldsymbol{\nabla}}\hat{\boldsymbol{u}})\, \hat{\boldsymbol{\Phi}}(\hat{\boldsymbol{\xi}}_{\mathrm{e}}) + \hat{\boldsymbol{\Phi}}(\hat{\boldsymbol{\xi}}_{\mathrm{e}})^{\mathrm{T}} (\hat{\boldsymbol{\nabla}}\hat{\boldsymbol{u}})^{\mathrm{T}} \right). \tag{10}$$

In the stress-free reference configuration $\hat{\Omega}_{\mathrm{f}} \cup \hat{\Omega}_{\mathrm{s}}$, the dynamical equilibrium between the Lagrangian solid (elastic stresses given by (3)) and the ALE fluid (viscous/pressure stresses given by (10)) is then written as follows [19,39,40]

$$\mathcal{M}_{\mathrm{s}} \frac{\partial^2 \hat{\boldsymbol{\xi}}_{\mathrm{s}}}{\partial t^2} = \hat{\boldsymbol{\nabla}} \cdot \hat{\mathbf{P}}(\hat{\boldsymbol{\xi}}_{\mathrm{s}}) = \mathbf{0} \quad \text{in} \quad \hat{\Omega}_{\mathrm{s}}, \tag{11}$$

$$\hat{\mathrm{J}}(\hat{\boldsymbol{\xi}}_{\mathrm{e}}) \frac{\partial \hat{\boldsymbol{u}}}{\partial t} + \left(\hat{\boldsymbol{\nabla}}\hat{\boldsymbol{u}}\, \hat{\boldsymbol{\Phi}}(\hat{\boldsymbol{\xi}}_{\mathrm{e}}) \right) \left(\hat{\boldsymbol{u}} - \frac{\partial \hat{\boldsymbol{\xi}}_{\mathrm{e}}}{\partial t} \right) - \hat{\boldsymbol{\nabla}} \cdot \hat{\boldsymbol{\Sigma}}(\hat{\boldsymbol{u}}, \hat{p}, \hat{\boldsymbol{\xi}}_{\mathrm{e}}) = \mathbf{0} \quad \text{in} \quad \hat{\Omega}_{\mathrm{f}}, \tag{12}$$

$$\hat{\boldsymbol{\nabla}} \cdot \left(\hat{\boldsymbol{\Phi}}(\hat{\boldsymbol{\xi}}_{\mathrm{e}})\, \hat{\boldsymbol{u}} \right) = 0 \quad \text{in} \quad \hat{\Omega}_{\mathrm{f}}, \tag{13}$$

$$\hat{\boldsymbol{u}} - \frac{\partial \hat{\boldsymbol{\xi}}_{\mathrm{s}}}{\partial t} = \mathbf{0} \quad \text{on} \quad \hat{\Gamma}, \tag{14}$$

$$\hat{\boldsymbol{\Sigma}}(\hat{\boldsymbol{u}}, \hat{p}, \hat{\boldsymbol{\xi}}_{\mathrm{e}})\, \hat{\boldsymbol{n}} - \hat{\mathbf{P}}(\hat{\boldsymbol{\xi}}_{\mathrm{s}}) \hat{\boldsymbol{n}} = \mathbf{0} \quad \text{on} \quad \hat{\Gamma}, \tag{15}$$

where (11) expresses the solid momentum conservation, Eqs. (12) and (13) express respectively the fluid momentum and mass conservations, while equations (14) and (15) express the continuity of the fluid and solid velocities and stresses at the fluid–solid interface $\hat{\Gamma}$. The extension field $\hat{\boldsymbol{\xi}}_{\mathrm{e}}$ is given by (6) and (7). The ALE formulation of the fluid–structure problem is completely defined once farfield boundary conditions, detailed later, are specified.

2.2. Modal stability analysis in the steady deformed configuration

Fluid–structure steady-states are time-independent solutions of the governing equations (6)–(15), denoted as

$$\hat{\boldsymbol{U}}(\hat{\boldsymbol{x}}), \quad \hat{P}(\hat{\boldsymbol{x}}), \quad \hat{\boldsymbol{\Xi}}_{\mathrm{s}}(\hat{\boldsymbol{x}}) \quad \text{and} \quad \hat{\boldsymbol{\Xi}}_{\mathrm{e}}(\hat{\boldsymbol{x}}), \tag{16}$$

for the velocity, pressure, solid displacement and extension displacement fields respectively. In that case, the fluid loads exactly balance the elastic restoring force so that the fluid–structure interface does not move. The fluid velocity is thus equal to zero at this interface and the velocity of the fluid domain in (12) also vanishes, i.e. $\partial\hat{\boldsymbol{\Xi}}_\mathrm{e}/\partial t = 0$. In the present study, the steady non-linear fluid–structure equations are solved with a Newton method. More details about the determination of these steady-state solutions are given in Appendix B and can also be found in other studies [41,42].

While the steady-state solutions are computed in the stress-free configuration, the linear stability analysis is performed in the steady deformed configuration, shown in the sketch in the right in Fig. 1. In this configuration, we note the quantities without superscripts. The fluid and solid domains are noted Ω_f and Ω_s respectively, while Γ is the fluid–solid interface. This configuration is obtained from the stress-free reference configuration by deformation by the steady displacement fields $\hat{\boldsymbol{\Xi}}_\mathrm{s}(\hat{\boldsymbol{x}})$ and $\hat{\boldsymbol{\Xi}}_\mathrm{e}(\hat{\boldsymbol{x}})$. The spatial position in $\Omega_\mathrm{f}\cup\Omega_\mathrm{s}$ is thus unequivocally defined as

$$\begin{aligned} &\boldsymbol{x}\in\Omega_\mathrm{s}\,, \quad \boldsymbol{x}=\hat{\boldsymbol{x}}+\hat{\boldsymbol{\Xi}}_\mathrm{s}(\hat{\boldsymbol{x}}) \quad \text{for} \quad \hat{\boldsymbol{x}}\in\hat{\Omega}_\mathrm{s},\\ &\boldsymbol{x}\in\Omega_\mathrm{e}\,, \quad \boldsymbol{x}=\hat{\boldsymbol{x}}+\hat{\boldsymbol{\Xi}}_\mathrm{e}(\hat{\boldsymbol{x}}) \quad \text{for} \quad \hat{\boldsymbol{x}}\in\hat{\Omega}_\mathrm{e}. \end{aligned} \tag{17}$$

New solid and extension displacement fields are then defined in this steady configuration, as $\boldsymbol{\xi}_\mathrm{s}(\boldsymbol{x},t)=\tilde{\boldsymbol{x}}_t-\boldsymbol{x}$ for $\boldsymbol{x}\in\Omega_\mathrm{s}$, and $\boldsymbol{\xi}_\mathrm{e}(\boldsymbol{x},t)=\tilde{\boldsymbol{x}}_t-\boldsymbol{x}$ for $\boldsymbol{x}\in\Omega_\mathrm{e}$. The fluid velocity and pressure fields are noted $\boldsymbol{u}$ and p respectively, they are obtained from their counterparts in the reference configuration through the variable change (17) as $\boldsymbol{u}(\boldsymbol{x})=\hat{\boldsymbol{u}}(\hat{\boldsymbol{x}})$ and $p(\boldsymbol{x})=\hat{p}(\hat{\boldsymbol{x}})$. The ALE formulation of the fluid–structure equations governing those variables is often referred to as an "updated Lagrangian" formulation [42], that is obtained by applying the change of coordinate (17) to the non-linear equations (11)–(15). By construction, the steady-state solutions expressed in the steady configuration are

$$(\boldsymbol{U},P)(\boldsymbol{x})=(\hat{\boldsymbol{U}},\hat{P})(\hat{\boldsymbol{x}}) \quad \text{and} \quad (\boldsymbol{\Xi},\boldsymbol{\Xi}_\mathrm{e})(\boldsymbol{x})=(\boldsymbol{0},\boldsymbol{0}). \tag{18}$$

While the updated formulation implies the presence of initial strains in the solid (as will be detailed later), in the fluid domain the fact that the steady displacements are zero greatly simplifies the linearized ALE formulation, for the steady deformation gradient operators just vanish.

To investigate the long-term stability of the steady-state solutions (18) in the steady deformed, pre-stressed configuration, we introduce the splitting

$$\begin{aligned} &(\boldsymbol{u},p)(\boldsymbol{x},t)=(\boldsymbol{U},P)(\boldsymbol{x})+\varepsilon\,\left((\boldsymbol{u}^\circ,p^\circ)(\boldsymbol{x})\,e^{(\lambda+\mathbf{i}\omega)t}+\text{c.c.}\right) \quad \text{in} \quad \Omega_\mathrm{f},\\ &(\boldsymbol{\xi}_\mathrm{s},\boldsymbol{\xi}_\mathrm{e})(\boldsymbol{x},t)=(\boldsymbol{0},\boldsymbol{0})+\varepsilon\,\left((\boldsymbol{\xi}_\mathrm{s}^\circ,\boldsymbol{\xi}_\mathrm{e}^\circ)(\boldsymbol{x})\,e^{(\lambda+\mathbf{i}\omega)t}+\text{c.c.}\right) \quad \text{in} \quad (\Omega_\mathrm{f},\Omega_\mathrm{s}), \end{aligned} \tag{19}$$

where ε is an arbitrary small real number, and the perturbation is decomposed into a modal form: λ and ω are the growth rate and angular frequency of the spatial structures $\boldsymbol{u}^\circ$, p°, $\boldsymbol{\xi}_\mathrm{s}^\circ$ and $\boldsymbol{\xi}_\mathrm{e}^\circ$ — which are complex fields, where "c.c." denotes the complex conjugate. By injecting this decomposition into the updated ALE formulation and keeping only the first-order terms in ε, one obtains the following eigenvalue problem:

$$(\lambda+\mathbf{i}\omega)\frac{\mathcal{M}_\mathrm{s}}{\hat{\mathrm{J}}(\hat{\boldsymbol{\Xi}}_\mathrm{s})}\boldsymbol{u}_\mathrm{s}^\circ=\boldsymbol{\nabla}\cdot\mathbf{P}'(\boldsymbol{\xi}_\mathrm{s}^\circ;\hat{\boldsymbol{\Xi}}_\mathrm{s}) \quad \text{in} \quad \Omega_\mathrm{s}, \tag{20}$$

$$\begin{aligned} (\lambda+\mathbf{i}\omega)\big(\boldsymbol{u}^\circ-(\boldsymbol{\nabla}\boldsymbol{U})\,\boldsymbol{\xi}_\mathrm{e}^\circ\big)&=\boldsymbol{\nabla}\cdot\Big[\boldsymbol{\Sigma}'(\boldsymbol{\xi}_\mathrm{e}^\circ,\boldsymbol{U},P)+\boldsymbol{\sigma}(\boldsymbol{u}^\circ,p^\circ)\Big]\ldots\\ &\quad-(\boldsymbol{\nabla}\boldsymbol{U})\boldsymbol{u}^\circ-(\boldsymbol{\nabla}\boldsymbol{u}^\circ)\boldsymbol{U}-(\boldsymbol{\nabla}\boldsymbol{U})\,\boldsymbol{\Phi}'(\boldsymbol{\xi}_\mathrm{e}^\circ)\,\boldsymbol{U} \quad \text{in} \quad \Omega_\mathrm{f}, \end{aligned} \tag{21}$$

$$0=\boldsymbol{\nabla}\cdot\boldsymbol{u}^\circ+\boldsymbol{\nabla}\cdot(\boldsymbol{\Phi}'(\boldsymbol{\xi}_\mathrm{e}^\circ)\,\boldsymbol{U}) \quad \text{in} \quad \Omega_\mathrm{f}, \tag{22}$$

$$\boldsymbol{0}=\boldsymbol{u}^\circ-\boldsymbol{u}_\mathrm{s}^\circ \quad \text{on} \quad \Gamma, \tag{23}$$

$$\boldsymbol{0}=\Big[\boldsymbol{\sigma}(\boldsymbol{u}^\circ,p^\circ)+\boldsymbol{\Sigma}'(\boldsymbol{\xi}_\mathrm{e}^\circ,\boldsymbol{U},P)\Big]\boldsymbol{n}-\mathbf{P}'(\boldsymbol{\xi}_\mathrm{s}^\circ;\hat{\boldsymbol{\Xi}}_\mathrm{s})\,\boldsymbol{n} \quad \text{on} \quad \Gamma, \tag{24}$$

where the spatial derivative operator is now $\boldsymbol{\nabla}=\partial/\partial\boldsymbol{x}$. The (complex) solid $\boldsymbol{u}_\mathrm{s}^\circ$ velocity field

$$(\lambda+\mathbf{i}\omega)\,\boldsymbol{\xi}_\mathrm{s}^\circ=\boldsymbol{u}_\mathrm{s}^\circ \quad \text{in} \quad \Omega_\mathrm{s} \tag{25}$$

is introduced so as to reduce the order of the temporal derivative in the solid equation. We choose here a Laplace equation for the extension operator, i.e.

$$\boldsymbol{0}=\boldsymbol{\nabla}^2\boldsymbol{\xi}_\mathrm{e}^\circ \quad \text{in} \quad \Omega_\mathrm{f}, \tag{26}$$

$$\mathbf{0} = \boldsymbol{\xi}_{\mathrm{e}}^{\circ} - \boldsymbol{\xi}_{\mathrm{s}}^{\circ} \qquad \text{on} \quad \Gamma. \tag{27}$$

In the solid equation (20), $\mathbf{P}'$ denotes the linearized first Piola–Kirchhoff stress tensor that writes in the steady deformed configuration as

$$\mathbf{P}'(\boldsymbol{\xi}_{\mathrm{s}}^{\circ}; \hat{\boldsymbol{\Xi}}_{\mathrm{s}}) = \frac{1}{\hat{\mathrm{J}}(\hat{\boldsymbol{\Xi}}_{\mathrm{s}})} \left\{ \nabla \boldsymbol{\xi}_{\mathrm{s}}^{\circ}\, \hat{\mathbf{F}}(\hat{\boldsymbol{\Xi}}_{\mathrm{s}})\, \hat{\mathbf{S}}(\hat{\boldsymbol{\Xi}}_{\mathrm{s}}) + \hat{\mathbf{F}}(\hat{\boldsymbol{\Xi}}_{\mathrm{s}})\, \mathbf{S}'(\boldsymbol{\xi}_{\mathrm{s}}^{\circ}; \hat{\boldsymbol{\Xi}}_{\mathrm{s}}) \right\} \hat{\mathbf{F}}(\hat{\boldsymbol{\Xi}}_{\mathrm{s}})^{\mathrm{T}}. \tag{28}$$

This expression involves in particular the steady strains $\hat{\mathbf{F}}(\hat{\boldsymbol{\Xi}}_{\mathrm{s}})$ that exist in the steady deformed configuration. The linearization of the second Piola–Kirchhoff stress tensor writes

$$\mathbf{S}'(\boldsymbol{\xi}_{\mathrm{s}}^{\circ}; \hat{\boldsymbol{\Xi}}_{\mathrm{s}}) = \lambda_s \operatorname{tr}\left(\mathbf{E}'(\boldsymbol{\xi}_{\mathrm{s}}^{\circ}; \hat{\boldsymbol{\Xi}}_{\mathrm{s}})\right) + 2\mu_s \mathbf{E}'(\boldsymbol{\xi}_{\mathrm{s}}^{\circ}; \hat{\boldsymbol{\Xi}}_{\mathrm{s}}), \tag{29}$$

$$\text{with} \quad \mathbf{E}'(\boldsymbol{\xi}_{\mathrm{s}}^{\circ}; \hat{\boldsymbol{\Xi}}_{\mathrm{s}}) = \frac{1}{2}\, \hat{\mathbf{F}}(\hat{\boldsymbol{\Xi}}_{\mathrm{s}})^{\mathrm{T}} \left(\nabla \boldsymbol{\xi}_{\mathrm{s}}^{\circ} + \nabla \boldsymbol{\xi}_{\mathrm{s}}^{\circ\mathrm{T}} \right) \hat{\mathbf{F}}(\hat{\boldsymbol{\Xi}}_{\mathrm{s}}). \tag{30}$$

If the strains in the steady-state solution are small, i.e. $\hat{\mathbf{F}}(\hat{\boldsymbol{\Xi}}_{\mathrm{s}}) \simeq \mathbf{I}$, then the linearized Saint-Venant–Kirchhoff law reduces to the classical linear elastic strain–stress relation and the solid equation (20) reduces to the linear elasticity equation. The fluid equations (21)–(22) involve the linearized deformation operator expressed in the steady deformed configuration as

$$\boldsymbol{\Phi}'(\boldsymbol{\xi}_{\mathrm{e}}^{\circ}) = \left(\nabla \cdot \boldsymbol{\xi}_{\mathrm{e}}^{\circ}\right) \mathbf{I} - \nabla \boldsymbol{\xi}_{\mathrm{e}}^{\circ}. \tag{31}$$

Note that the linearization of the deformation operator (8) in the stress-free reference configuration yields to a more complicated expression, involving additional terms related to the steady deformation field $\hat{\boldsymbol{\Xi}}_{\mathrm{e}}(\hat{\boldsymbol{x}})$. In the steady deformed configuration, these contributions are directly taken into account by the deformation of the domain itself, thus greatly simplifying the expression of the linearized fluid problem. In the momentum equation (21) there are terms linearized with respect to the fluid velocity and pressure (which are identical to what is obtained in a rigid case), plus additional terms that represent how the steady equilibrium $(\boldsymbol{U}, P)$ is affected by the domain displacement perturbation. An extra term related to the geometry modification is also present in the mass conservation equation (22). In (21), $\boldsymbol{\sigma}$ is the classical (viscous) Cauchy stress tensor

$$\boldsymbol{\sigma}(\boldsymbol{u}^{\circ}, p^{\circ}) = -p^{\circ}\, \mathbf{I} + \frac{1}{\mathcal{R}_{\mathrm{e}}} \left(\nabla \boldsymbol{u}^{\circ} + \nabla \boldsymbol{u}^{\circ\mathrm{T}} \right) \tag{32}$$

while the linearization of the fluid stress tensor (9) with respect to the extension displacement field writes, in the steady deformed configuration, as

$$\boldsymbol{\Sigma}'(\boldsymbol{\xi}_{\mathrm{e}}^{\circ}, \boldsymbol{U}, P) = \boldsymbol{\sigma}(\boldsymbol{U}, P) \boldsymbol{\Phi}'(\boldsymbol{\xi}_{\mathrm{e}}^{\circ})^{\mathrm{T}} - \frac{1}{\mathcal{R}_{\mathrm{e}}} \left(\nabla \boldsymbol{U}\, \nabla \boldsymbol{\xi}_{\mathrm{e}}^{\circ} + (\nabla \boldsymbol{\xi}_{\mathrm{e}}^{\circ})^{\mathrm{T}} (\nabla \boldsymbol{U})^{\mathrm{T}} \right). \tag{33}$$

More details on the linearization steps can be found in [25,27,40] for instance.

2.3. Spatial discretization

The eigenvalue problem (20)–(27) is discretized in space with the finite-element method. The continuous Galerkin weak formulation of the modal problem is obtained by multiplying each equation with test functions belonging to the appropriate functional space and integrating over the appropriate spatial domain. Following the three-field discrete formulation proposed by [5], all the variables and test-functions (noted with the symbol $\boldsymbol{\psi}$) are gathered into three sub-groups, namely the solid, fluid and extension variables, as follows:

$$\begin{aligned}
&\boldsymbol{q}_{\mathrm{s}}^{\circ} = \left(\boldsymbol{\xi}_{\mathrm{s}}^{\circ}, \boldsymbol{u}_{\mathrm{s}}^{\circ}\right), && \boldsymbol{\psi}_{\mathrm{s}} = \left(\boldsymbol{\psi}_{\mathrm{s}}^{\boldsymbol{\xi}}, \boldsymbol{\psi}_{\mathrm{s}}^{\boldsymbol{u}}\right), && \text{in } \mathcal{U}^{\mathrm{s}} \times \mathcal{U}^{\mathrm{s}},\\
&\boldsymbol{q}_{\mathrm{f}}^{\circ} = \left(\boldsymbol{u}^{\circ}, p^{\circ}, \boldsymbol{\lambda}^{\circ}\right), && \boldsymbol{\psi}_{\mathrm{f}} = \left(\boldsymbol{\psi}^{\boldsymbol{u}}, \psi^{p}, \boldsymbol{\psi}^{\boldsymbol{\lambda}}\right), && \text{in } \mathcal{U}^{\mathrm{f}} \times \mathcal{P}^{\mathrm{f}} \times \mathcal{U}^{\Gamma},\\
&\boldsymbol{q}_{\mathrm{e}}^{\circ} = \left(\boldsymbol{\xi}_{\mathrm{e}}^{\circ}, \boldsymbol{\lambda}_{\mathrm{e}}^{\circ}\right), && \boldsymbol{\psi}_{\mathrm{e}} = \left(\boldsymbol{\psi}_{\mathrm{e}}^{\boldsymbol{\xi}}, \boldsymbol{\psi}_{\mathrm{e}}^{\boldsymbol{\lambda}}\right), && \text{in } \mathcal{U}^{\mathrm{e}} \times \mathcal{U}^{\Gamma}.
\end{aligned}$$

The solid variable $\boldsymbol{q}_{\mathrm{s}}^{\circ}$ gathers the solid velocity and displacement, that both belong to the functional space $\mathcal{U}^{\mathrm{s}} = \{\boldsymbol{u} \in \mathcal{H}^1(\Omega_{\mathrm{s}})^d, \boldsymbol{u} = \mathbf{0} \text{ on } \Gamma_{\mathrm{s}}^D\}$ where Γ_{s}^D denotes the boundary of the solid domain Ω_{s} where Dirichlet boundary conditions are applied and $d = 2, 3$ depending on the dimension of the problem.

The fluid variable $\boldsymbol{q}_{\mathrm{f}}^{\circ}$ regroups the velocity and pressure, as well as a new variable $\boldsymbol{\lambda}^{\circ}$ defined on the fluid–solid interface Γ. Classically, the fluid velocity is taken in the functional space $\mathcal{U}^{\mathrm{f}} = \{\boldsymbol{u} \in \mathcal{H}^1(\Omega_{\mathrm{f}})^d, \boldsymbol{u} = \mathbf{0} \text{ on } \Gamma_{\mathrm{f}}^D\}$ [43],

and Γ_{f}^{D} denotes the boundary of the fluid domain Ω_{f} where Dirichlet boundary conditions are applied. The fluid pressure is taken in $\mathcal{P}^{\mathrm{f}} = \mathcal{L}^2(\Omega_{\mathrm{f}})$, while the supplementary variable $\boldsymbol{\lambda}^\circ$ belongs to $\mathcal{U}^{\Gamma} = \{\boldsymbol{v} \in \mathcal{H}^{-1/2}(\Gamma)^d\}$. This additional variable is a Lagrange multiplier that allows for the stress continuity (24) to be satisfied in a weak sense [44], as a result of the duality with a weak imposition of the velocity continuity condition (23) as

$$\mathbf{0} = \int_{\Gamma} \left(\boldsymbol{u}^\circ - \boldsymbol{u}_{\mathrm{s}}^\circ\right) \cdot \boldsymbol{\psi}^{\boldsymbol{\lambda}} \mathrm{d}\Gamma \qquad \forall\, \boldsymbol{\psi}^{\boldsymbol{\lambda}} \in \mathcal{U}^{\Gamma}.$$

To clarify how the velocity Lagrange multiplier $\boldsymbol{\lambda}^\circ$ arises in the weak formulation, let us consider the fluid momentum equation (21) and integrate by parts the conservative terms, yielding

$$\begin{aligned}
&\int_{\Omega_{\mathrm{f}}} \left(\boldsymbol{\nabla} \cdot \left(\boldsymbol{\sigma}(\boldsymbol{u}^\circ, p^\circ) + \boldsymbol{\Sigma}'(\boldsymbol{\xi}_{\mathrm{s}}^\circ, \boldsymbol{U}, P)\right)\right) \cdot \boldsymbol{\psi}^{\boldsymbol{u}} \,\mathrm{d}\Omega = \\
&- \int_{\Omega_{\mathrm{f}}} \left(\boldsymbol{\sigma}(\boldsymbol{u}^\circ, p^\circ) + \boldsymbol{\Sigma}'(\boldsymbol{\xi}_{\mathrm{s}}^\circ, \boldsymbol{U}, P)\right) : \boldsymbol{\nabla} \boldsymbol{\psi}^{\boldsymbol{u}} \,\mathrm{d}\Omega + \int_{\Gamma} \boldsymbol{\lambda}^\circ \cdot \boldsymbol{\psi}^{\boldsymbol{u}} \,\mathrm{d}\Gamma
\end{aligned}$$

where in the integrand of the boundary integral in the right-hand side the velocity Lagrange multiplier is introduced as $\boldsymbol{\lambda}^\circ = (\boldsymbol{\sigma}(\boldsymbol{u}^\circ, p^\circ) + \boldsymbol{\Sigma}'(\boldsymbol{\xi}_{\mathrm{s}}^\circ, \boldsymbol{U}, P))(-\boldsymbol{n})$. The Lagrange multiplier unknown thus gives the linearized normal stress at the interface (recall that $\boldsymbol{n}$ points from the solid to the fluid domain, see Fig. 1). Turning now to the solid equations, we obtain

$$\int_{\Omega_{\mathrm{s}}} \boldsymbol{\nabla} \cdot \mathbf{P}'(\boldsymbol{\xi}_{\mathrm{s}}^\circ; \hat{\boldsymbol{\Xi}}_{\mathrm{s}}) \cdot \boldsymbol{\psi}_{\mathrm{s}}^{\boldsymbol{u}} \,\mathrm{d}\Omega = - \int_{\Omega_{\mathrm{s}}} \mathbf{P}'(\boldsymbol{\xi}_{\mathrm{s}}^\circ; \hat{\boldsymbol{\Xi}}_{\mathrm{s}}) : \boldsymbol{\nabla} \boldsymbol{\psi}_{\mathrm{s}}^{\boldsymbol{u}} \,\mathrm{d}\Omega - \int_{\Gamma} \boldsymbol{\lambda}^\circ \cdot \boldsymbol{\psi}_{\mathrm{s}}^{\boldsymbol{u}} \,\mathrm{d}\Gamma$$

where we have also replaced the linearized normal solid stress in the boundary integral by the velocity Lagrange multiplier using the stress continuity condition (24), i.e. $\boldsymbol{\lambda}^\circ = \mathbf{P}'(\boldsymbol{\xi}_{\mathrm{s}}^\circ)(-\boldsymbol{n})$. The introduction of the velocity Lagrange multiplier in the weak formulations of both fluid and solid equations thus allows to enforce (24) in a completely implicit way [43].

The extension variable $\boldsymbol{q}_{\mathrm{e}}^\circ$ is composed of the extension displacement $\boldsymbol{\xi}_{\mathrm{e}}^\circ$ and a second Lagrange multiplier $\boldsymbol{\lambda}_{\mathrm{e}}^\circ$. The extension displacement is taken in the functional space $\boldsymbol{\xi}_{\mathrm{e}}^\circ \in \mathcal{U}^{\mathrm{e}} = \{\boldsymbol{u} \in \mathcal{H}^1(\Omega_{\mathrm{e}})^d,\ \boldsymbol{u} = 0 \text{ on } \partial\Omega_{\mathrm{e}} \setminus \Gamma\}$ where the extension domain Ω_{e} is a subset of the fluid domain Ω_{f}, that encloses the solid as represented in Fig. 6. The extension displacement can be extended by continuity and set to zero in the fluid domain outside the extension domain, where the ALE fluid equation thus reduces to the pure hydrodynamic equations. This strategy allows to reduce the overall computational cost, as will be detailed in Section 3.3. Like the velocity Lagrange multiplier, $\boldsymbol{\lambda}_{\mathrm{e}}^\circ$ is defined on the fluid–solid interface and is taken in $\mathcal{U}^{\Gamma}$. It is associated to the weak formulation of the fluid and solid displacement continuity condition (27), namely

$$\mathbf{0} = \int_{\boldsymbol{\Gamma}} \left(\boldsymbol{\xi}_{\mathrm{e}}^\circ - \boldsymbol{\xi}_{\mathrm{s}}^\circ\right) \cdot \boldsymbol{\psi}_{\mathrm{e}}^{\boldsymbol{\lambda}} \,\mathrm{d}\Gamma.$$

Note that $\boldsymbol{\lambda}_{\mathrm{e}}^\circ$ only intervenes in the weak formulation of the extension problem, where it is introduced to replace the "pseudo-stress" exerted by the extension displacement at the fluid–solid interface, i.e. $\boldsymbol{\lambda}_{\mathrm{e}}^\circ = (\boldsymbol{\nabla}\boldsymbol{\xi}_{\mathrm{e}}^\circ)(-\boldsymbol{n})$. This allows to satisfy the displacement continuity without having in return a feedback of the extension pseudo-stress on the physical stresses [45].

The three-fields weak formulation of the coupled fluid–structure perturbation eigenvalue problem is finally written whatever $\boldsymbol{\psi}_{\mathrm{s}} \in \mathcal{U}^{\mathrm{s}} \times \mathcal{U}^{\mathrm{s}}$, $\boldsymbol{\psi}_{\mathrm{e}} \in \mathcal{U}^{\mathrm{e}} \times \mathcal{U}^{\Gamma}$ and $\boldsymbol{\psi}_{\mathrm{f}} \in \mathcal{U}^{\mathrm{f}} \times \mathcal{P}^{\mathrm{f}} \times \mathcal{U}^{\Gamma}$ as

$$(\lambda + \mathbf{i}\omega)\, \mathcal{B}_{\mathrm{s}}(\boldsymbol{\psi}_{\mathrm{s}}, \boldsymbol{q}_{\mathrm{s}}^\circ) = \mathcal{A}_{\mathrm{s}}(\boldsymbol{\psi}_{\mathrm{s}}, \boldsymbol{q}_{\mathrm{s}}^\circ) + \mathcal{A}_{\mathrm{fs}}(\boldsymbol{q}_{\mathrm{f}}^\circ, \boldsymbol{\psi}_{\mathrm{s}}), \tag{34}$$

$$\mathbf{0} = \mathcal{A}_{\mathrm{e}}(\boldsymbol{\psi}_{\mathrm{e}}, \boldsymbol{q}_{\mathrm{e}}^\circ) + \mathcal{A}_{\mathrm{es}}(\boldsymbol{\psi}_{\mathrm{e}}, \boldsymbol{q}_{\mathrm{s}}^\circ), \tag{35}$$

$$(\lambda + \mathbf{i}\omega) \left\{\mathcal{B}_{\mathrm{f}}(\boldsymbol{\psi}_{\mathrm{f}}, \boldsymbol{q}_{\mathrm{f}}^\circ) + \mathcal{B}_{\mathrm{fe}}(\boldsymbol{\psi}_{\mathrm{f}}, \boldsymbol{q}_{\mathrm{e}}^\circ)\right\} = \mathcal{A}_{\mathrm{f}}(\boldsymbol{\psi}_{\mathrm{f}}, \boldsymbol{q}_{\mathrm{f}}^\circ) + \mathcal{A}_{\mathrm{fs}}(\boldsymbol{\psi}_{\mathrm{f}}, \boldsymbol{q}_{\mathrm{s}}^\circ) + \mathcal{A}_{\mathrm{fe}}(\boldsymbol{\psi}_{\mathrm{f}}, \boldsymbol{q}_{\mathrm{e}}^\circ). \tag{36}$$

The expression of the different operators involved in the three equations above is given in Appendix A. The weak formulations (34), (35) and (36) are spatially discretized onto unstructured meshes. The meshes of the solid Ω_{s} and fluid Ω_{f} domains are generated with a conformal discretization of the common fluid–solid interface Γ. For $d = 2$ (resp. $d = 3$), these meshes are composed of triangles (resp. tetrahedra). The discrete counterpart of the extension subdomain $\Omega_{\mathrm{e}} \subset \Omega_{\mathrm{f}}$ is defined as a simply-connected subset of the elements enclosing the fluid–solid boundary, so that in the common domain $\Omega_{\mathrm{e}} \cap \Omega_{\mathrm{f}}$ the extension and fluid vertices are exactly located at the same position. Details on the procedure of triangles selection are given in Section 3.3. Quadratic Lagrange elements P_2 are used for the

fluid velocity and the solid/extension displacement, while linear Lagrange elements P_1 are used for the pressure and the Lagrange multipliers so as to satisfy the Ladyzhenskaya–Babuška–Brezzi condition [46].

The discrete generalized eigenvalue problem obtained from (34), (35) and (36) is then

$$(\lambda + \mathbf{i}\omega) \begin{bmatrix} \mathbf{B}_\mathrm{s} & 0 & 0 \\ 0 & 0 & 0 \\ 0 & \mathbf{B}_\mathrm{fe} & \mathbf{B}_\mathrm{f} \end{bmatrix} \begin{bmatrix} \boldsymbol{q}_\mathrm{s}^\circ \\ \boldsymbol{q}_\mathrm{e}^\circ \\ \boldsymbol{q}_\mathrm{f}^\circ \end{bmatrix} = \begin{bmatrix} \mathbf{A}_\mathrm{s} & 0 & \mathbf{A}_\mathrm{fs}^\mathrm{T} \\ \mathbf{A}_\mathrm{es} & \mathbf{A}_\mathrm{e} & 0 \\ \mathbf{A}_\mathrm{fs} & \mathbf{A}_\mathrm{fe} & \mathbf{A}_\mathrm{f} \end{bmatrix} \begin{bmatrix} \boldsymbol{q}_\mathrm{s}^\circ \\ \boldsymbol{q}_\mathrm{e}^\circ \\ \boldsymbol{q}_\mathrm{f}^\circ \end{bmatrix}, \tag{37}$$

where $\mathbf{A}_\mathrm{s}$, for instance, denotes the matrix resulting from the spatial discretization of the operator $\mathcal{A}_\mathrm{s}$, etc. The left-hand side matrix is not symmetric due to the off-diagonal term $\mathbf{B}_\mathrm{fe}$, obtained from the temporal derivative of the extension displacement. A symmetric formulation can nevertheless be obtained at the price of introducing an additional extension velocity variable $\boldsymbol{u}_\mathrm{e}^\circ = \sigma\, \boldsymbol{\xi}_\mathrm{e}^\circ$. In the first line (solid equation), the off-diagonal term $\mathbf{A}_\mathrm{fs}^\mathrm{T}$ results from the continuity of the fluid and solid velocities at the interface and expresses the coupling with the fluid. In the second line (extension equation), the off-diagonal term $\mathbf{A}_\mathrm{es}$ results from the continuity of the extension and solid displacements at the fluid–solid interface. In the last line (fluid equation), the off-diagonal term $\mathbf{A}_\mathrm{fs}$ also results from the continuity of the fluid and solid velocities at the interface, while $\mathbf{A}_\mathrm{fe}$ represents the shape derivatives of the fluid equation. The finite-element software FreeFem++ [47] is used to assemble the sparse block matrices in the above eigenvalue problem. Finally, it should be noted that the eigenmodes are normalized so that $\boldsymbol{q}_\mathrm{s}^{\circ\mathrm{H}} \mathbf{B}_\mathrm{s} \boldsymbol{q}_\mathrm{s}^\circ = 1$, where the superscript H denotes the transconjugate operation.

2.4. Reduced eigenvalue problem

To reduce the number of degrees of freedom in the above eigenvalue problem, that might be very large when considering a finer mesh resolution and three-dimensional configurations, we can eliminate the extension displacement, that depends only on the solid displacement according to

$$\boldsymbol{q}_\mathrm{e}^\circ = -\mathbf{A}_\mathrm{e}^{-1} \mathbf{A}_\mathrm{es}\, \boldsymbol{q}_\mathrm{s}^\circ. \tag{38}$$

By introducing this expression into (37), one obtains the smaller problem

$$(\lambda + \mathbf{i}\omega) \begin{bmatrix} \mathbf{B}_\mathrm{f} & -\mathbf{B}_\mathrm{fe}\mathbf{A}_\mathrm{e}^{-1}\mathbf{A}_\mathrm{es} \\ 0 & \mathbf{B}_\mathrm{s} \end{bmatrix} \begin{bmatrix} \boldsymbol{q}_\mathrm{f}^\circ \\ \boldsymbol{q}_\mathrm{s}^\circ \end{bmatrix} = \begin{bmatrix} \mathbf{A}_\mathrm{f} & \mathbf{A}_\mathrm{fs} - \mathbf{A}_\mathrm{fe}\mathbf{A}_\mathrm{e}^{-1}\mathbf{A}_\mathrm{es} \\ \mathbf{A}_\mathrm{fs}^\mathrm{T} & \mathbf{A}_\mathrm{s} \end{bmatrix} \begin{bmatrix} \boldsymbol{q}_\mathrm{f}^\circ \\ \boldsymbol{q}_\mathrm{s}^\circ \end{bmatrix}, \tag{39}$$

in which the extension variable has disappeared, at the price of the inverted operator $\mathbf{A}_\mathrm{e}^{-1}$ appearing in the upper right corners of the block matrices that form the reduced problem. Consequently, the matrices in the above reduced eigenvalue problem are very expensive to assemble and their inversion cannot be performed with a sparse LU factorization, since $\mathbf{A}_\mathrm{e}^{-1}$ is in general a full, large-scale matrix. To circumvent this difficulty, one possibility is to resort to a projection of the solid equations onto the free-vibration modal basis truncated to N_s modes. Projecting the solid dynamics on this basis, the projection of the off-diagonal operators $\mathbf{A}_\mathrm{fe}\mathbf{A}_\mathrm{e}^{-1}\mathbf{A}_\mathrm{es}$ and $\mathbf{B}_\mathrm{fe}\mathbf{A}_\mathrm{e}^{-1}\mathbf{A}_\mathrm{es}$ can be assembled explicitly, as we will detail hereafter. Eventually, we then obtain an *approximate* problem (the solid is reduced to a few vibration modes) having the size of the fluid problem only, plus the number of vibration modes.

The free-vibration modes, denoted $\boldsymbol{\phi}_{\mathrm{s},k}^\circ$ for $k = 1, 2, \ldots$, are the vibration modes of the solid structure in absence of dynamic coupling with the fluid — the static coupling resulting from the steady deformed equilibrium is however embedded in the matrices $\mathbf{B}_\mathrm{s}$ and $\mathbf{A}_\mathrm{s}$. They are obtained as eigenvectors of the eigenvalue problem

$$\mathbf{i}\omega_{\mathrm{s},k}\, \mathbf{B}_\mathrm{s}\, \boldsymbol{\phi}_{\mathrm{s},k}^\circ = \mathbf{A}_\mathrm{s}\, \boldsymbol{\phi}_{\mathrm{s},k}^\circ \tag{40}$$

that corresponds to the solid sub-problem extracted from (37), and where the coupling $\mathbf{A}_\mathrm{fs}^\mathrm{T}$ with the fluid is cancelled out. In this problem (and in the supposed case where there are no unstable static buckling modes), the associated eigenvalues $\mathbf{i}\omega_{\mathrm{s},k}$ are purely imaginary, where $\omega_{\mathrm{s},k}$ is the vibration circular frequency of the mode k. By normalizing the free-vibrations modes as ${\boldsymbol{\phi}_{\mathrm{s},k}^\circ}^\mathrm{T}\, \mathbf{B}_\mathrm{s}\, \boldsymbol{\phi}_{\mathrm{s},k}^\circ = 1$, they form an orthonormal basis that is used to decompose the solid component of the eigenvectors $\boldsymbol{q}_\mathrm{s}^\circ$ onto a finite number N_s of free-vibration modes, as

$$\boldsymbol{q}_\mathrm{s}^\circ = \sum_{k=1}^{N_s} \alpha_{\mathrm{s},k}\, \boldsymbol{\phi}_{\mathrm{s},k}^\circ = \boldsymbol{\Phi}_\mathrm{s}\, \boldsymbol{\alpha}_\mathrm{s}. \tag{41}$$

The columns of the rectangular matrix $\boldsymbol{\Phi}_\mathrm{s} = \left[\boldsymbol{\phi}^\circ_{\mathrm{s},1}, \boldsymbol{\phi}^\circ_{\mathrm{s},2}, \ldots, \boldsymbol{\phi}^\circ_{\mathrm{s},N_s}\right]$ are the free-vibration modes and $\boldsymbol{\alpha}_s = (\alpha_{s,1}, \alpha_{s,2}, \ldots, \alpha_{s,N_s})^\mathrm{T}$ denotes the vector of modal amplitudes. Introducing this decomposition into (39) and projecting orthogonally onto the free-vibration basis, one obtains the reduced eigenvalue problem

$$(\lambda + \mathbf{i}\omega) \begin{bmatrix} \mathbf{B}_\mathrm{f} & \mathbf{B}^r_\mathrm{fs} \\ 0 & \mathbf{B}^r_\mathrm{s} \end{bmatrix} \begin{bmatrix} \boldsymbol{q}^\circ_\mathrm{f} \\ \boldsymbol{\alpha}_\mathrm{s} \end{bmatrix} = \begin{bmatrix} \mathbf{A}_\mathrm{f} & \mathbf{A}^r_\mathrm{fs} \\ \mathbf{A}^r_\mathrm{sf} & \mathbf{A}^r_\mathrm{s} \end{bmatrix} \begin{bmatrix} \boldsymbol{q}^\circ_\mathrm{f} \\ \boldsymbol{\alpha}_\mathrm{s} \end{bmatrix}, \tag{42}$$

where the superscript r is used to indicate the reduced matrices defined as

$$\begin{aligned} &\mathbf{B}^r_\mathrm{s} = {\boldsymbol{\Phi}_\mathrm{s}}^\mathrm{T} \mathbf{B}_\mathrm{s} \boldsymbol{\Phi}_\mathrm{s}\,, \quad \mathbf{A}^r_\mathrm{s} = {\boldsymbol{\Phi}_\mathrm{s}}^\mathrm{T} \mathbf{A}_\mathrm{s} \boldsymbol{\Phi}_\mathrm{s}\,, \quad \mathbf{A}^r_\mathrm{sf} = (\mathbf{A}_\mathrm{fs}\boldsymbol{\Phi}_\mathrm{s})^\mathrm{T}, \\ &\mathbf{B}^r_\mathrm{fs} = -\mathbf{B}_\mathrm{fe}\,\mathbf{A}_\mathrm{e}^{-1}\mathbf{A}_\mathrm{es}\boldsymbol{\Phi}_\mathrm{s}\,, \quad \mathbf{A}^r_\mathrm{fs} = (\mathbf{A}_\mathrm{fs} - \mathbf{A}_\mathrm{fe}\,\mathbf{A}_\mathrm{e}^{-1}\mathbf{A}_\mathrm{es})\boldsymbol{\Phi}_\mathrm{s}. \end{aligned} \tag{43}$$

These are small matrices, that are therefore easy to assemble, even if they are not sparse. $\mathbf{B}^r_\mathrm{s}$ and $\mathbf{A}^r_\mathrm{s}$ are diagonal matrices of size $N_s \times N_s$. The free-vibrations modes forming an orthonormal basis, the first reduced matrix reduces to the identity matrix, i.e. $\mathbf{B}^r_\mathrm{s} = \mathbf{I}^r$. By definition of the free-vibration modes (40), the diagonal coefficients of $\mathbf{A}^r_\mathrm{s}$ are the free-vibration frequencies $\omega_{\mathrm{s},k}$ with $1 \leq k \leq N_s$. The off-diagonal reduced matrices are rectangular. $\mathbf{A}^r_\mathrm{fs}$ is obtained by performing N_s times the product of $\mathbf{A}_\mathrm{fs}$ with the free-vibration modes. The assembly of the off-diagonal matrices $\mathbf{B}^r_\mathrm{fs}$ and $\mathbf{A}^r_\mathrm{fs}$ is slightly more complicated. For each free-vibration mode $\boldsymbol{\phi}^\circ_{\mathrm{s},k}$, an extension displacement mode $\boldsymbol{\phi}^\circ_{\mathrm{e},k}$ is obtained by solving

$$\mathbf{A}_\mathrm{e}\boldsymbol{\phi}^\circ_{\mathrm{e},k} = \mathbf{A}_\mathrm{es}\ \boldsymbol{\phi}^\circ_{\mathrm{s},k}. \tag{44}$$

By performing the matrix–vector product $-\mathbf{B}_\mathrm{fe}\,\boldsymbol{\phi}^\circ_{\mathrm{e},k}$, one obtains the kth column of the matrix $\mathbf{B}^r_\mathrm{fs}$. By performing the matrix–vector products $\mathbf{A}_\mathrm{fe}\,\boldsymbol{\phi}^\circ_{\mathrm{e},k}$ and $\mathbf{A}_\mathrm{fs}\,\boldsymbol{\phi}^\circ_{\mathrm{s},k}$ and taking the difference, one obtains the kth column of the matrix $\mathbf{A}^r_\mathrm{fs}$.

The eigenvalues/eigenvectors obtained with the reduced eigenproblem are approximations of the eigenvalues/eigenvectors obtained with the full eigenproblem, since the solid dynamics are projected onto a reduced basis of free-vibration modes. In Section 3, the accuracy of this approximation is assessed in Section 3.4, otherwise the full eigenproblem is considered to perform the stability analysis.

2.5. Resolution of eigenvalue problems and practical implementation

The full and reduced generalized eigenvalue problems (37) and (42) are formally rewritten

$$\sigma\,\mathbf{B}\,\mathbf{q}^\circ = \mathbf{A}\,\mathbf{q}^\circ \tag{45}$$

where $\sigma = \lambda + \mathbf{i}\omega$ denotes the complex eigenvalue associated to the eigenvector $\mathbf{q}^\circ$. The components of this eigenvector and the definition of the matrices $\mathbf{B}$ and $\mathbf{A}$ depend on the eigenvalue problem considered. In both cases, we are interested by computing the leading eigenvalues, i.e. those with the largest growth rate λ. To that aim, a shift-and-invert spectral transformation is applied to (45), yielding the transformed eigenvalue problem

$$\sigma_s\,\mathbf{q}^\circ = \left(\mathbf{A} - s\mathbf{B}\right)^{-1}\mathbf{B}\,\mathbf{q}^\circ \tag{46}$$

where s is the so-called complex shift and σ_s are the shifted eigenvalues. The eigenvectors are identical in the transformed and original eigenvalue problems, while the eigenvalues are related through the relation $\sigma_s = 1/(\sigma - s)$. The shifted eigenvalues σ_s of largest magnitude correspond to the closest eigenvalues σ from the shift s. To determine the portion of the spectrum displaying the eigenvalues with the largest growth-rate, the eigenproblem is solved for several values of s close to the real axis, spanning the imaginary axis in a range of frequency where unstable eigenvalues are expected.

The Implicitly Restarted Arnoldi Method (IRAM) implemented in the library ARPACK [48] is used to compute the eigenvalues. This library is called from the finite-element software FreeFem++ [47], interfaced with ARPACK library. The reverse communication interface of the latter requires, when using the shift-and-invert mode, to perform the matrix–vector product $\mathbf{B}\mathbf{q}_i$ and to solve the following linear problem, for any input vector $\mathbf{q}_i$,

$$(\mathbf{A} - s\mathbf{B})\mathbf{q}_o = \mathbf{q}_i \tag{47}$$

The finite-element software FreeFem++ [47] is used to assemble the large scale sparse matrices $\mathbf{B}$ and $\mathbf{A}$, as well as to solve the above linear problem. More precisely, the MUMPS library [49] is used to perform a sparse LU

decomposition of the shifted matrix $\mathbf{A} - s\mathbf{B}$ and to apply the Lower and Upper triangular resolution. The slow LU decomposition is performed once for all, unlike the fast upper and lower resolutions which are performed as many times as required by the IRAM algorithm. This strategy is efficient for eigenvalue problems with a small number of degrees of freedom, but is limited by the large amount of memory needed to perform the LU decomposition. To solve eigenvalue problems with a large number of degrees of freedom, an iterative resolution of the shifted problem is preferred, based on the Gauss–Seidel block preconditioner [43] of the fluid–structure matrix.

To summarize, the linear stability analysis of fluid–solid steady solutions is a two-steps process that consists in determining first the steady solution, and secondly the eigenmodes of largest growth rate that develop over this steady solution.

Computing the steady solution: The steady deformed solution is obtained by solving with a Newton method the steady equations (6)–(15) written in the stress-free reference configuration $\hat{\Omega}$. Details on the non-linear steady solver are given in Appendix B.

Computing the leading eigenvalues: They can be obtained by solving either the full (37) or the reduced (42) eigenproblem. In both cases, the mesh of the steady deformed configuration Ω is computed by deforming the mesh of the reference configuration $\hat{\Omega}$ using the steady displacement fields $\hat{\boldsymbol{\Xi}}_\mathrm{s}$ and $\hat{\boldsymbol{\Xi}}_\mathrm{e}$. Once the steady solid strains are computed in the reference configuration, they are pushed forward on the deformed configuration, together with the steady velocity and pressure fields.

Full eigenvalue problem. To obtain the leading eigenvalues/eigenvectors of (37) in the vicinity of the shift s, we proceed as follow:

1. The following block matrices are assembled with FreeFem++: the constant matrices $\mathbf{B}_\mathrm{f}$, $\mathbf{A}_\mathrm{es}$, $\mathbf{A}_\mathrm{e}$, $\mathbf{A}_\mathrm{fs}$, the matrices $\mathbf{B}_\mathrm{fe}$, $\mathbf{A}_\mathrm{fe}$, $\mathbf{A}_\mathrm{f}$ that depend on the steady velocity and pressure, and the matrices $\mathbf{A}_\mathrm{s}$, $\mathbf{B}_\mathrm{s}$ that depend on the steady strains.
2. the eigenvalue problem (37) is solved with the shift-and-invert approach described above.
   - for small-scale eigenvalue problems (typically for cases with a number of degrees of freedom less than about 5×10^{10}), the matrices $\mathbf{B}$ and $\mathbf{A} - s\mathbf{B}$ are first assembled. A single direct LU decomposition of the shifted matrix $\mathbf{A} - s\mathbf{B}$ is then performed. For each right-hand side vector $\mathbf{q}_i$ provided by the IRAM algorithm, the shifted linear problem (47) is solved by performing successively the lower and an upper triangular resolution.
   - for larger-scale eigenvalue problems, a single direct LU decomposition of each block matrix $\mathbf{A}_\mathrm{s} - s\mathbf{B}_\mathrm{s}$, $\mathbf{A}_\mathrm{f} - s\mathbf{B}_\mathrm{f}$ and $\mathbf{A}_\mathrm{e}$ is first performed. For each right-hand side vector $\mathbf{q}_i$ provided by the IRAM algorithm, the shifted linear problem (47) is solved iteratively with the GMRES algorithm preconditioned by a block Gauss–Seidel preconditioner [43].

Reduced eigenvalue problem. When the solid dynamics may be described with a few (N_s) free-vibrations modes, solving the reduced eigenproblem (42) is advantageous. This can be done as follows:

1. Compute N_s free-vibration modes $\boldsymbol{\phi}^\circ_{\mathrm{s},k}$, solutions of the free-vibration eigenproblem (40).
2. Perform a single LU decomposition of the matrix $\mathbf{A}_\mathrm{e}$ and compute N_s extension modes $\boldsymbol{\phi}^\circ_{\mathrm{e},k}$, solutions of (44).
3. Assemble first the reduced matrices $\mathbf{A}^r_{sf}$, $\mathbf{A}^r_{fs}$ and $\mathbf{B}^r_{fs}$ defined in (43), and then the matrix $\mathbf{B}$ and shifted matrix $\mathbf{A} - s\mathbf{B}$ corresponding to the reduced eigenproblem (42).
4. the leading eigenvalue of the reduced eigenvalue problem (42) is then obtained with the shift-and-invert approach described above. A single direct LU decomposition of the shifted $\mathbf{A} - s\mathbf{B}$ is performed. The shifted linear problem (47) is then solved at each iteration of the IRAM algorithm, with fast lower and upper triangular resolutions.

The FreeFem++ scripts allowing the computation of the non-linear steady solutions and leading eigenmodes will be made available on the website https://w3.onera.fr/erc-aeroflex/.

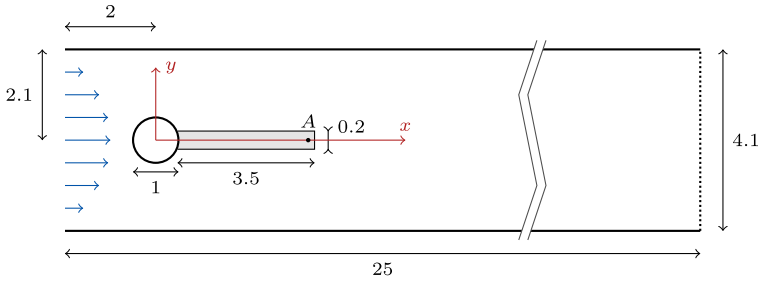

Fig. 2. Reference configuration for the vortex-induced elastic-deformation instability. Sketch of the geometry proposed by [29] with the associated non-dimensional lengths. Point A is located in the elastic plate at the position $(x_A, y_A) = (3.95, 0)$ in the reference configuration.

3. Results

In this section, we first present numerical results obtained for two significant two-dimensional test-cases corresponding to the flow induced vibrations of an elastic bar, and of the flutter instability of a flag in a channel flow. In the first case, the fluid–structure instability is essentially driven by the fluid wake instability, whereas in the second configuration the fluid–solid interaction is essential for the development of the instability. A three-dimensional configuration is finally considered, that consists in the vortex shedding instability in the wake of a plate deflected by the steady flow.

3.1. Test case with a vortex-induced-deformation instability

The first test case considered here is the configuration proposed and used by Turek & Hron [29] for benchmarking steady and unsteady nonlinear fluid–structure interaction solvers. As shown in Fig. 2, an elastic plate is clamped at the rear of a rigid circular cylinder of diameter D^*, which is placed in a channel flow, with a parabolic velocity profile imposed at the inlet. The centre of the cylinder is not located on the symmetry axis of the channel, but is slightly shifted downwards, thus creating an asymmetry in the fluid–solid solution. Details of the geometry are indicated in Fig. 2, where all lengths have been made non-dimensional using the cylinder's diameter as reference length $L^* = D^*$. The mean velocity of the parabolic velocity profile, denoted $\bar{U}^*$, is chosen as the reference velocity, i.e. $U^* = \bar{U}^*$. Values of the four non-dimensional parameters defined in (1) and characterizing this fluid–structure problem are chosen as

$$120 \leq \mathcal{R}_e \leq 220\,,\ \mathcal{M}_s = 1\,,\ \mathcal{E}_s = 1400\,,\ \nu_s = 0.4. \tag{48}$$

When considering the Reynolds number $\mathcal{R}_e = 200$, we retrieve the test-case denoted FSI3 in [29]. At the maximal value of the Reynolds number, as shown in the following, multiple unstable eigenvalues are obtained. Smaller values of the Reynolds number are also considered, so as to have cases with only a single unstable eigenvalue with a moderate growth-rate, making it possible to monitor the growth of the instability over several periods using non-linear simulations.

The unsteady ALE equations (11) to (15) written in the reference configuration are satisfied with the following boundary conditions. The non-dimensional parabolic velocity profile $u = 0.357\,(2 + y)\,(2.1 - y)$ is imposed at the inlet of the channel. The no-slip boundary conditions $(u, v) = (0, 0)$ are imposed at the top and bottom walls, as well as on the surface of the rigid cylinder (denoted Γ_{cyl}). At the outlet of the channel, a zero normal-stress boundary condition is imposed. The non-linear unsteady ALE solver is also implemented in the FreeFem++ software and a validation is provided in Appendix B. When solving these equations for the above values of the non-dimensional parameters, one systematically obtains a periodic solution, that is characterized by the unsteady shedding of vortices in the flow and an unsteady deformation of the elastic plate. Such a configuration can be referred to as a *vortex-induced deformation* configuration [3], since the vortex-shedding in the wake of the rigid cylinder induces the deformation of the elastic plate.

As explained in Section 2.2, steady solutions of (11) to (15) are computed by solving the steady equations using a Newton method. More details on the numerical algorithm are given in Appendix B. Starting from a uniform zero field as initial guess, a steady solution is first computed at Reynolds number $\mathcal{R}_e = 20$. This solution is then used as

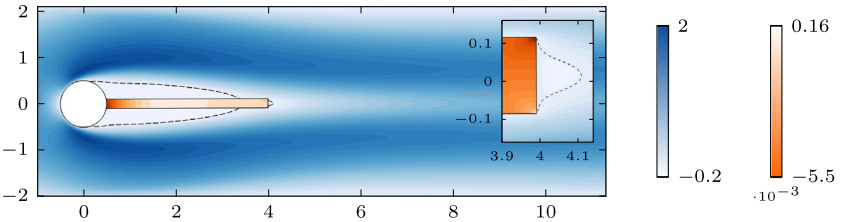

Fig. 3. Steady solution for the vortex-induced-deformation test case, shown in the steady deformed configuration, $\mathcal{R}_e = 120$. The streamwise component of the velocity $\boldsymbol{U}$ of the steady flow is depicted in blue, while the shear component $[\hat{\mathbf{F}}(\hat{\boldsymbol{\Xi}}_s)]_{xy}$ of the strain tensor is depicted in orange in the elastic plate. The dashed lines delimit the recirculating flow regions (a zoom on the tip end of the plate is represented in the inset on the right, where the orange colour has also been modified to emphasize the peaks at the corners, compared to the full picture). (For interpretation of the references to colour in this figure legend, the reader is referred to the web version of this article.)

initial guess in the Newton algorithm to compute the steady solution at $\mathcal{R}_e = 120$. For that value of the Reynolds number, the Newton algorithm allows to converge towards this steady solution, that cannot been determined by marching in time the unsteady equations, since it is unstable (as shown later). Steady solutions at higher Reynolds numbers are computed similarly. Note that, it was not necessary to use any stabilization techniques to ensure the numerical stability of the finite-element discretization (at least up to $\mathcal{R}_e = 220$), probably because the steady solutions are smooth enough for the low values of the Reynolds number considered here. The fluid velocity (blue) and the shear component $[\hat{\mathbf{F}}(\hat{\boldsymbol{\Xi}}_s)]_{xy}$ of the solid strain tensor (orange) are shown in Fig. 3. Although barely visible due to the small deformation of the solid, the visualization is done in the steady deformed configuration, obtained after having deformed the domain using the steady displacement field. The steady flow separates on the rigid cylinder and reattaches on the elastic plate, as indicated by the black dashed curves which represent the isocontours of zero streamwise velocity. The two recirculation regions formed on the upper and lower sides of the elastic plate are not symmetric with respect to the symmetry axis of the channel, due to the slight asymmetry of the cylinder's position in this channel. The recirculation velocity is slightly larger in the upper region than in the lower region, thus creating a resultant pressure force that moves the elastic plate upward. The y-displacement of the point A (located at $y = 0$ in the reference configuration) is around 0.015, as reported in Table 1. The flow recirculation also generates viscous shear forces oriented upstream and resulting in a slight compression of the elastic plate. The x-displacement is however two orders of magnitude lower than the y-displacement and is therefore not reported here. Finally, the drag and lift coefficients of the rigid cylinder plus the elastic plate are computed as

$$\mathcal{C}_D = 2\int_{\hat{\Gamma}\cup\Gamma_{cyl}} \hat{\boldsymbol{\Sigma}}(\hat{\boldsymbol{U}},\hat{P},\hat{\boldsymbol{\Xi}}_e)\hat{\boldsymbol{n}}\cdot\mathbf{e}_x\,\mathrm{d}\hat{\Gamma} \quad \text{and} \quad \mathcal{C}_L = 2\int_{\hat{\Gamma}\cup\Gamma_{cyl}} \hat{\boldsymbol{\Sigma}}(\hat{\boldsymbol{U}},\hat{P},\hat{\boldsymbol{\Xi}}_e)\hat{\boldsymbol{n}}\cdot\mathbf{e}_y\,\mathrm{d}\hat{\Gamma},$$

where $\hat{\Gamma}$ denotes the fluid-elastic plate boundary and Γ_{cyl} the rigid cylinder surface and $\hat{\boldsymbol{\Sigma}}$ is given in (9). They are equal to $\mathcal{C}_D = 2.533$ and $\mathcal{C}_L = 8.53 \times 10^{-3}$, the weak positive lift being induced by the slight asymmetry of the configuration. The influence of the mesh resolution on the computed steady-state solution is reported in Table 1, which shows the drag coefficient and the y-displacement of the elastic plate at point A. The drag coefficient as well as the plate displacement reach converged values for the mesh labelled M_3. More details about the validation of the non-linear steady solver are reported in Appendix B.

The linear stability analysis of the steady solution is investigated by solving the eigenvalue problem (37). The eigenvalue spectrum obtained for $\mathcal{R}_e = 120$ is displayed in Fig. 4(a) and exhibits one unstable pair of complex eigenvalues ($\lambda > 0, \omega \neq 0$). The real and imaginary parts of the corresponding eigenvector are displayed in Fig. 4(b). The transverse solid displacement field inside the elastic plate is depicted in orange, while the arrows represent the centreline displacement vectors. The mode presents a spatial structure in the solid with one vibration node at the clamped end of the plate. When the phase of the mode is varied between 0 and 2π, a second vibration minima moves back and forth along the centreline of the plate (see an animation of the mode in supplementary material).

The influence of the spatial resolution on the unstable eigenvalues is reported in the sixth column in the Table 1. A converged eigenvalue is reached as the mesh resolution is increased. The unstable eigenvalues are compared with estimations of the growth rate and frequency (reported in the last column of the table) obtained by marching in time the non-linear unsteady ALE equations written in the reference configuration. To estimate the growth rate

Table 1
Vortex-induced deformation test-case at $\mathcal{R}_e = 120$. The total number of elements and the minimal size of the elements are indicated in the second and third columns respectively. The drag coefficient is given in the fourth columns. The fifth column reports the transverse solid displacement at point A located in $x_A = 3.95$, $y_A = 0$ in the reference configuration. The sixth column reports the value of the leading complex-conjugate eigenvalues, while the last column reports the growth-rate and angular frequency extracted from time-marching non-linear simulations in the linear phase.

Mesh	N_t	Δy	C_D	$\xi_y^s(A)$	Eigenvalue	Time-march
M_0	3 264	0.113	2.440	0.0163	$-0.023 \pm 1.674\mathbf{i}$	Steady-state
M_1	8 788	0.051	2.516	0.0158	$0.0226 \pm 1.689\mathbf{i}$	(0.0228, 1.688)
M_2	15 716	0.030	2.528	0.0152	$0.0237 \pm 1.688\mathbf{i}$	(0.0238, 1.688)
M_3	32 732	0.018	2.531	0.0155	$0.0238 \pm 1.688\mathbf{i}$	(0.0238, 1.687)
M_4	59 689	0.012	2.533	0.0154	$0.0238 \pm 1.688\mathbf{i}$	–

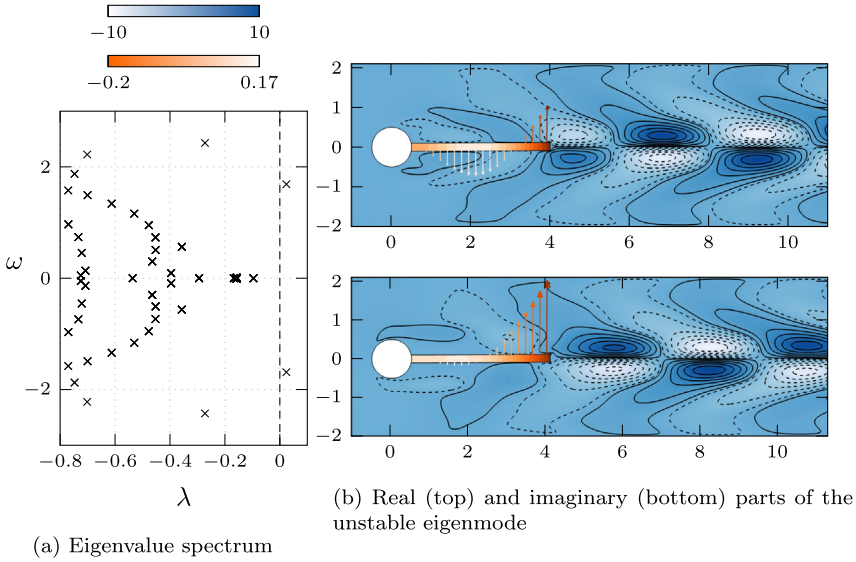

(a) Eigenvalue spectrum

(b) Real (top) and imaginary (bottom) parts of the unstable eigenmode

Fig. 4. Results of the stability analysis for the vortex-induced elastic-deformation configuration with non-dimensional parameters (48) and $\mathcal{R}_e = 120$. (a) Eigenvalue spectrum. The eigenvalues are displayed with crosses in the plane (λ, ω) (growth rate, frequency). The vertical dashed line delimits the (left) stable half-plane from the (right) unstable half-plane. Numerical values of the unstable eigenvalues are reported in Table 1 for different mesh resolutions. (b) Snapshots of the unstable mode eigenvector for the real (top) and imaginary (bottom) parts, depicted with the streamwise component of the fluid velocity (blue, dashed negative contours), and the transverse solid displacement (orange). The centreline displacement in the solid is represented by the orange arrows. Results obtained with the mesh M_4. (For interpretation of the references to colour in this figure legend, the reader is referred to the web version of this article.)

and frequency of the *linear* perturbation using the unsteady non-linear solver, the initial solution is chosen as the superposition of the steady solution and of the Lagrangian perturbation mode, scaled with a small amplitude $a = 0.005$ here. The amplitude of the perturbation is expected to grow exponentially as long as it is small enough so that the non-linear terms are negligible. Fig. 5 depicts the absolute value of the lift coefficient of the fluctuation as a function of time, equal to the lift coefficient of the unsteady solution corrected by the steady lift coefficient $\mathcal{C}_{\mathrm{L_{stat.}}}$. For $t < 200$, the fluctuating lift coefficient grows exponentially (straight envelope in the log-scale) and the estimated growth rate is in good agreement with the growth-rate λ of the eigenvalue analysis, given by the slope of the red line in the figure. The Fourier spectra of the signal in the linear phase show one largely predominant peak. The resulting frequencies are reported in the last column of Table 1, showing a good agreement.

When increasing the Reynolds number, the mode previously described (for $\mathcal{R}_e = 120$) becomes more unstable. Increasing the Reynolds number up to $\mathcal{R}_e = 200$ (benchmark case FSI3 from Turek and Hron [29]), computing the corresponding steady flow and running the eigenvalue analysis, one observes that the leading pair of complex eigenvalues is $0.298 \pm 1.814\,\mathbf{i}$ (mesh M4). A second pair of complex eigenvalues gets unstable for a critical value

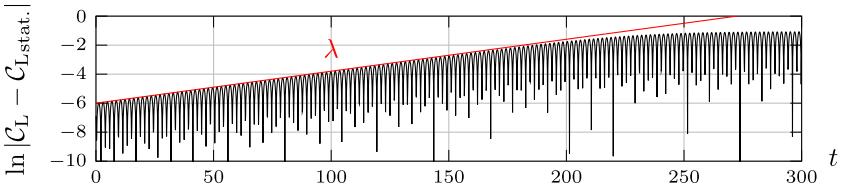

Fig. 5. Results obtained with temporal simulation for $\mathcal{R}_e = 120$, where the initial condition is the superposition of the steady solution and the unstable eigenmode found in Fig. 4a with an amplitude $a = 0.005$. Representation of the absolute value of the lift coefficient for the cylinder and the plate as a function of time, and superimposed growth rate λ given by the eigenvalue analysis After $t \simeq 250$, a periodic limit-cycle is reached.

in Reynolds number interval between 215 and 220. For $\mathcal{R}_e = 220$, the two pairs of unstable eigenvalues are $0.365 \pm 1.861\mathbf{i}$ and $0.0047 \pm 2.313\,\mathbf{i}$ on mesh M4.

In the configuration of a splitter plate clamped to a rigid cylinder, a vortex-shedding may occur in the wake flow even when the splitter plate is rigid ($\mathcal{E}_s \to \infty$). The unsteadiness is due to a purely hydrodynamic eigenmode that gets unstable when the Reynolds number is high enough. Such fluid–structure configurations are referred to as vortex-induced vibration configurations, since the vortex-shedding in the flow induces the vibration of the elastic solid. Although the fluid–structure coupling may be so strong that the vortex-induced vibration can occur for sub-critical values of the Reynolds number [50], the fluid–solid coupling is not uniquely responsible for the appearance of unsteadiness. On the other hand, the flutter of slender elastic bodies, like high aspect ratio wings or flags, is an unsteady aero-elastic phenomenon that is solely induced by the fluid–solid interaction [3]. The next section is devoted to the analysis of a two-dimensional test case exhibiting a flag flutter instability.

3.2. Test case with a flag flutter instability

The test case considered in this paragraph is shown in Fig. 6 and is similar to the configuration investigated by Cisonni et al. [30]. A thin elastic plate, denoted "flag" hereinafter, is clamped at the rear of a rigid plate of same thickness, and placed at the centre of a channel flow. All lengths have been made non-dimensional using the height of the channel H^* as the reference length ($L^* = H^*$). Identical parabolic velocity profiles are imposed at the two inlets of the channel, and their mean velocity is chosen as the reference velocity (i.e. $U^* = U^*$). Following [30], we impose $u(y) = 12y(1-2y)$ at the upper inlet and $u(y) = -12y(1+2y)$ at the lower inlet. The four non-dimensional parameters governing this problem are defined with these reference quantities and their values are

$$\mathcal{E}_s = 13766\ ,\ \nu_s = 0.4\ ,\ \mathcal{M}_s = 25\ ,\ \mathcal{R}_e = 100 \tag{49}$$

These values of the non-dimensional elastic Young modulus $\mathcal{E}_s$, Poisson coefficient ν_s, density ratio ρ and Reynolds number $\mathcal{R}_e$ correspond to the reduced velocity $U = 13.53$ and the inertia ratio $M = 4$ used as a set of non-dimensional parameters in [30]. The non-dimensional lengths are indicated in Fig. 6, in particular the aspect ratio of the flag is $h_L = 1/100$ (corresponding to the case labelled (vii) in Figure 7a in [30]). The relations between the different parametrizations are given by $\mathcal{M}_s = 1/(Mh_L)$ and $\mathcal{E}_s = 12(1-\nu_s^2)/(h_L^3 MU^2)$. No-slip boundary conditions are imposed on the top and bottom walls, as well as on the surface of the rigid and elastic plates. At the outlet of the channel, a zero normal-stress boundary condition is imposed. When solving the unsteady non-linear fluid–structure equations for these values of the non-dimensional parameters, the flag oscillates around its mean deformed position and unsteady flow oscillations develop downstream [30]. The onset of the oscillations is attributed to a flutter instability which is triggered by the energy transfer from the fluid to the solid [3]. In particular, unlike in the previous case, there is no pre-existing fluid instability in the wake in the range of Reynolds number investigated.

The steady-state solution is computed with the methodology already described in the previous paragraph with an additional ingredient: the symmetry of the present configuration with respect to channel's axis is used to determine the steady-state solution, by imposing a zero transverse displacement condition along the centreline of the solid. The steady-state solution is depicted in Fig. 7 with the streamwise fluid velocity (blue) and the axial component $[\hat{\mathbf{F}}(\hat{\boldsymbol{\Xi}}_s)]_{xx}$ of the solid strain tensor (orange). The main difference with the vortex-induced deformation configuration

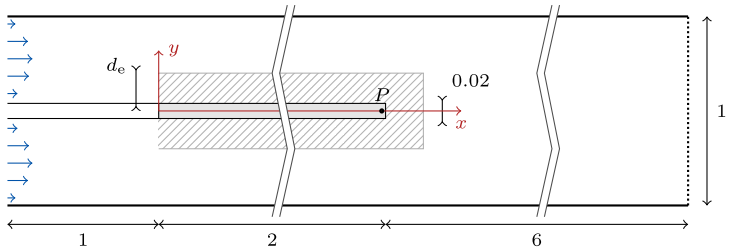

Fig. 6. Reference configuration for the flutter instability. Sketch of the geometry investigated by [30]. The dashed rectangular box is the extension domain Ω^e, and the reference point P is located at the position $(1.95, 0)$.

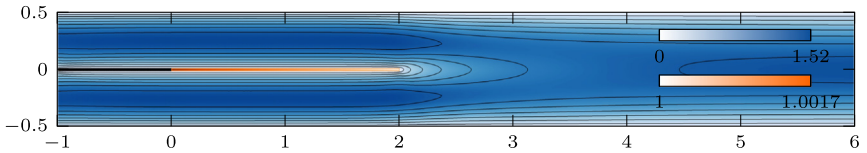

Fig. 7. Steady-state solution in the flutter instability configuration. Streamwise fluid velocity is depicted in blue while the component $[\hat{\mathbf{F}}(\hat{\boldsymbol{\Xi}}_s)]_{xx}$ of the solid strain tensor is shown in orange. (For interpretation of the references to colour in this figure legend, the reader is referred to the web version of this article.)

investigated before is that the steady flow does not separate from the solid surface, except at the trailing edge of the flag where a tiny recirculation region appears (its length is less than the thickness of the flag). The viscous fluid forces produce a slight stretching of the flag. This can be observed in Fig. 7 where the axial stress is maximal at the clamped end of the flag, then decreases as we move closer to the tip. The drag coefficient exerted on the flag $\mathcal{C}_{\mathrm{D}}^{f}$, and the solid axial displacement $(\boldsymbol{\Xi}_P \cdot \mathbf{e_x})$ of point $P(1.95, 0)$, are reported in Table 2 for various mesh resolutions. Both the drag coefficient and the solid displacement, which is of order of magnitude of 10^{-3}, do not display significant evolution for meshes finer than M_2.

The linear stability of this steady-state solution is now investigated. A converged eigenvalue spectra is depicted in Fig. 8a. A pair of complex unstable eigenvalues is found close to the imaginary axis. The spatial structure of the corresponding eigenvector is shown in Fig. 8b. It displays four vibration minimas in the solid, which are emphasized in Fig. 8c where the y component of the transverse displacement perturbation $\boldsymbol{\xi}'(y, 0) = \mathrm{Real}(\boldsymbol{\xi}_s^{\circ}(y, 0) \exp \mathbf{i}\phi)$ is represented for different phases ϕ varying between 0 and 2π. The resulting superposition shows the vibration envelope. A first vibration node is obviously located at the clamped end $x_0 = 0$. Then, a second vibration node is clearly noticeable at a position x_1. The third and fourth vibration minimas in x_2 and x_3 (see the positions in Fig. 8d) cannot be assimilable to vibration nodes, since the position of zero transverse displacement varies with the phase (see in supplementary material an animation showing the mode). In Fig. 8d the position of the vibration minimas of the leading eigenmode is reported, together with measurements made on the modal shapes extracted from non-linear simulations in [30], also represented by orange dots in Fig. 8c. A very good agreement is found concerning the position x_1. Since the other vibration minima are less marked (and thus less identifiable as vibration nodes), the evaluation of their position is less relevant. An estimate is nevertheless given in Fig. 8d. The influence of the spatial resolution on the leading eigenvalue is reported in Table 2. Compared to the vortex-induced-deformation test-case, the spatial resolution needs to be finer for converging the growth rate and the frequency.

We compare now the instability thresholds predicted with the eigenvalue analysis to those reported by [30] and obtained with time-marching simulations. In this study, the authors vary different parameters such as the plate aspect ratio, the mass ratio M or the reduced velocity U. Then, neutral curves are determined by running non-linear time-marching simulations in which a small-amplitude perturbation is applied at the flag at the beginning of the computation. The growth (resp. decay) of the oscillations is measured so as to estimate an unstable (resp. stable) growth-rate of the perturbations. The vibration frequencies are estimated using a Fast Fourier Transform of the oscillation signal at the tip end of the flag.

In what follows, the Reynolds number, Poisson coefficient and inertia ratio are fixed to the values used previously, (i.e. $\mathcal{R}_e = 100$, $\nu_s = 0.4$ and $M = 4$), while the reduced velocity U is varied — in this case, this amounts to varying

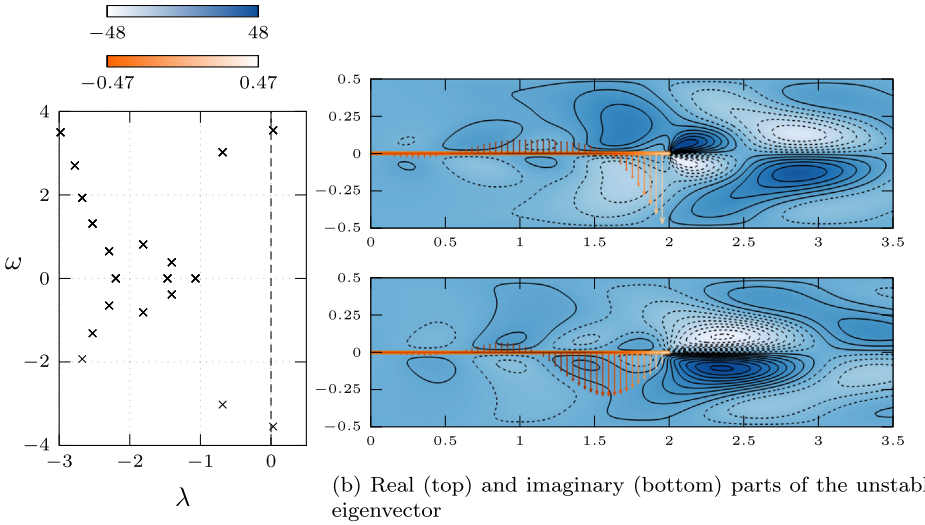

(a) Spectrum

(b) Real (top) and imaginary (bottom) parts of the unstable eigenvector

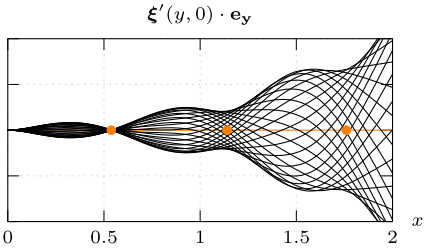

(c) Solid centreline transverse displacement

node	lin. stab.	ref. [30]
x_1	0.54	0.54
x_2	1.12	1.14
x_3	1.70	1.76

(d) Positions of the vibration nodes in the solid

Fig. 8. Flutter-induced vibrations case. (a) Eigenvalue spectra. (b) Real and imaginary parts of the leading eigenmode depicted with the streamwise fluid velocity (blue, dashed negative contours) and the transverse solid velocity (orange). (c) Solid transverse displacement extracted along the centreline ($y = 0$) of the solid, for 25 phases varying between 0 and 2π. Orange dots represent the vibrations minimas found in [30] also reported in (d). Results are shown for the finer mesh. (For interpretation of the references to colour in this figure legend, the reader is referred to the web version of this article.)

Table 2
Flutter-induced elastic-deformation test-case. The total number of elements N_t and the minimal/maximal size of the elements are indicated in the second and third/fourth columns. The fifth and sixth columns display the drag coefficient of the flag and the streamwise displacement at point P. The leading complex-conjugate eigenvalue is reported in the last column.

Mesh	N_t	$\Delta^{\max}$	$\Delta^{\min}$	$\mathcal{C}_{\mathrm{D}}^{\mathrm{f}}$	$\boldsymbol{\Xi}_P \cdot \mathbf{e}_{\mathbf{x}}$	Eigenvalue
M_0	3 675	0.1649	0.0164	1.016	1.663×10^{-3}	$0.0210 \pm 3.530\,\mathbf{i}$
M_1	8 899	0.1335	0.0109	1.017	1.668×10^{-3}	$0.0294 \pm 3.534\,\mathbf{i}$
M_2	16 105	0.0942	0.0081	1.015	1.670×10^{-3}	$0.0280 \pm 3.542\,\mathbf{i}$
M_3	35 272	0.0720	0.0038	1.016	1.671×10^{-3}	$0.0297 \pm 3.545\,\mathbf{i}$
M_4	67 602	0.0517	0.0025	1.016	1.672×10^{-3}	$0.0305 \pm 3.546\,\mathbf{i}$

only the stiffness of the plate. The results are reported in Fig. 9. On the left side, the growth-rate of the leading eigenvalue is displayed as a function of the reduced velocity U, while the angular frequency is reported on the right side. The case $(U, M) = (13.53, 4)$, or equivalently $(\mathcal{E}_s, \mathcal{M}_s) = (13766, 25)$ is the reference flutter case presented in Fig. 6, and is materialized by the dashed vertical line. The linear stability analysis predicts an instability threshold $(\lambda = 0)$ for $U^{\mathrm{crit}} = 13.35 \pm 0.05$, which is very close to the one obtained by Cisonni et al. [30] at $U = 13.53$. The frequency at the threshold is estimated from [30] to $\omega^{\mathrm{crit}} = 3.5 \pm 0.1$ (their values are reported in a logarithmic

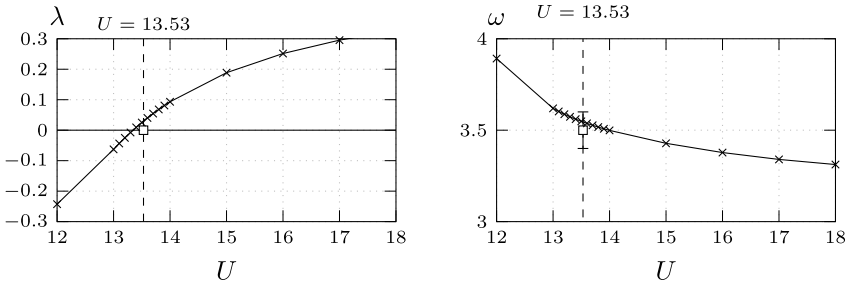

Fig. 9. Flutter-induced vibrations, evolution of the leading eigenvalue for a mass ratio $M = 4$, Reynolds number $\mathcal{R}_e = 100$ and Poisson coefficient $\nu_s = 0.4$ when the reduced velocity U is varied, with mesh M_3. The values corresponding to the flutter-induced case studied earlier in this paper is marked with the dashed line (parameters $M = 4$ and $U = 13.53$). The values obtained by Cisonni et al. are reported with squares symbols: the instability onset is found to $U = 13.53$ (left), with a vibration frequency estimated around 3.5 ± 0.1 (right).

scale on a figure). Once again, the frequency prediction obtained with the linear approach is in good agreement. It is interesting to notice that the computational time for the characterization of one case is estimated to about 1.2 hours on an Intel Xeon X5660 2.8 GHz processor (CPUmark score 7622 according to www.cpubenchmark.net, where it is claimed that the score roughly scales linearly with the amount of data that the processor can handle in a given period of time). In our sequential computations, performed with one core of an Intel Xeon E5-1620 v3 3.5 GHz processor (CPUmark score 9758), it takes about 2 minutes to compute a steady flow and then about 4 minutes to compute 20 eigenvalues on the mesh M_3 with the Lagrangian approach (without the modal projection evoked in Section 3.4). This clearly shows the advantage of running linear analyses for thresholds identifications.

As a conclusion, our linear eigenvalue analysis, tested in a strongly coupled case where the instability arises primarily from the fluid–structure coupling, is able to reproduce at much lower costs the instability thresholds obtained with non-linear time-marching simulations. In the next two sections, we evaluate the influence of the extension equation on the results, as well as the modal projection approach presented in Section 2.4.

3.3. Influence of the extension operator and domain

The ALE formulation introduces a non-physical variable, the extension displacement, to propagate the solid displacement field at the fluid–solid boundary into the fluid domain with the extension operator. In the present linear stability analysis, the perturbation of the extension displacement $\boldsymbol{\xi}_e^\circ$ is by definition infinitesimal and is thus never used to explicitly move the fluid domain, unlike in non-linear simulations. Nevertheless, we investigate here the influence of the extension domain size on the results of the linear stability analysis.

Due to the infinitesimal size of the extension displacement, we expect that the extension domain can be reduced to a few layers of elements around the elastic solid, as depicted in the sketch of Fig. 6. The extension region, depicted with dashed lines, extends over a layer of thickness d_e around the solid. For a given mesh, we define the signed distance function $\delta(\boldsymbol{x})$ of any point $\boldsymbol{x} \in \Omega_f$ from the fluid–solid boundary Γ. The extension mesh Ω_e is then defined as the set of elements whose centroids satisfy the relation $\delta(\boldsymbol{x}) < d_e$. Thus d_e controls the thickness of the extension domain and the number N_L of layers of elements, without changing the distribution of the elements in the fluid mesh. This way of proceeding allows one to study only the influence of the size of the extension domain, without changing the overall mesh resolution.

The characteristics of the extension regions and their influence on the leading eigenmode are reported in Table 3. The extension region does not influence the leading eigenvalue provided its size is sufficiently large, $d_e > 0.2$ in the present case. Note also the greater sensitivity of the growth-rate: while the frequency varies by about 0.03 % between the case $d_e = 0.199$ and $d_e = 0.38$, the variation is by 1.3 % for the growth-rate. For the case with only one layer, the discrepancy compared to the converged values is by 41 % for the growth-rate, and a remarkably small 0.84 % for the frequency. We have also performed the same tests on the vortex-induced elastic deformation case, and observed the same behaviour, with even smaller variations, probably due to the fact that the instability mechanism is essentially linked with the wake located further downstream to the interface.

Let us now examine the eigenvectors, and more specifically the absolute value of the streamwise fluid velocity. This quantity is displayed in Fig. 10 with solid lines, for two sizes of the extension domain, $d_e = 0.4$ (top) and

Table 3
Characteristics of the extension domain and influence on the leading eigenmodes. d_e is the thickness of the extension domain Ω_e, while N_L and N_{Ω_e} are the numbers of layers of triangles and the total number of triangles in the extension region, respectively. The leading complex-conjugate eigenvalue is reported in the last column.

d_e	N_L	N_{Ω^e}	Eigenvalue
0.500	>15	17 475	$0.0297 \pm 3.545\,\mathbf{i}$
0.380	>15	15 721	$0.0297 \pm 3.545\,\mathbf{i}$
0.199	12	13 829	$0.0301 \pm 3.544\,\mathbf{i}$
0.041	6	8 421	$0.0320 \pm 3.541\,\mathbf{i}$
0.018	3	5 444	$0.0341 \pm 3.536\,\mathbf{i}$
0.010	2	3 531	$0.0364 \pm 3.530\,\mathbf{i}$
0.005	1	1 793	$0.0419 \pm 3.515\,\mathbf{i}$

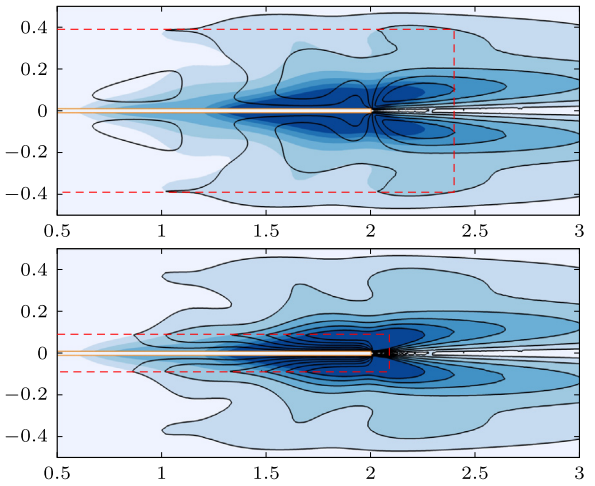

Fig. 10. Influence of the extension domain on the spatial structure of the leading eigenmode for (top) $d = 0.4$ and (bottom) $d = 0.1$. The limit of the extension region is marked with the red dashed line. Contours correspond to the module of the streamwise Lagrangian velocity ($|\boldsymbol{u}^\circ \cdot \mathbf{e_x}|$) while colours represent the Eulerian velocity $|\tilde{\boldsymbol{u}}^\circ \cdot \mathbf{e_x}|$, defined in (50).

$d_e = 0.01$ (bottom). A strong difference is observed inside the extension domain, while the isocontours look the same outside this region. This is expected since $\boldsymbol{u}^\circ$ is the Lagrangian velocity perturbation that depends on the extension displacement $\boldsymbol{\xi}_e^\circ$. To display a quantity independent on the extension displacement, we follow Fernandez and Le Tallec [19] and define the Eulerian-based velocity perturbation as

$$\tilde{\boldsymbol{u}}^\circ = \boldsymbol{u}^\circ - \boldsymbol{\nabla U}\, \boldsymbol{\xi}_e^\circ \tag{50}$$

that includes the effect of the transport by the domain movement of the steady flow. Such an Eulerian-based perturbation is displayed with colours in Fig. 10. A comparison between the two figures shows that the spatial structure of the Eulerian velocity does not depend on the size of the extension domain.

To conclude, the size of the extension domain cannot be reduced to very few layers around the solid domain, without modifying significantly the results of the stability analysis. The critical size of the extension region depends on the mesh resolution at the interface but also on the problem investigated: all things being equal, it is for instance smaller in the vortex-induced-deformation problem than in the flutter problem, probably because the origin of the instability is more critically the fluid–solid interaction in the latter case. As explained and detailed in Section 3.4, the extension displacement field variable can also be eliminated from the discrete eigenvalue problem, to the price of projecting the solid dynamics on a reduced basis composed of free-vibration modes. Results obtained with the resulting reduced eigenvalue problem are presented in the next paragraph.

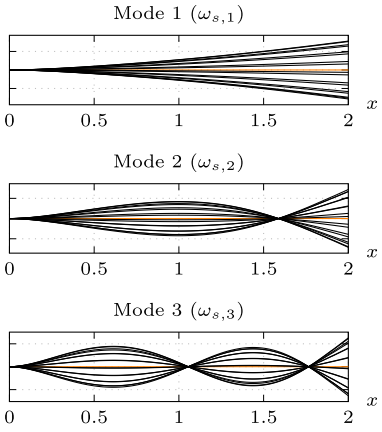

(a) mode shapes

N_s	Eigenvalue	T_{LU}
1	$-2.760 \pm 2.761\,\mathbf{i}$	0.22
2	$-0.856 \pm 2.085\,\mathbf{i}$	0.21
3	$0.1860 \pm 2.848\,\mathbf{i}$	0.21
4	$0.0078 \pm 3.972\,\mathbf{i}$	0.21
5	$0.0360 \pm 3.581\,\mathbf{i}$	0.22
10	$0.0289 \pm 3.546\,\mathbf{i}$	0.23
20	$0.0296 \pm 3.545\,\mathbf{i}$	0.26
Full	$0.0297 \pm 3.545\,\mathbf{i}$	1

(b) coupled eigenvalues

Fig. 11. Flutter-induced case, free vibration modes. (a) Snapshots of the transverse centreline displacement in the solid for different phases, for the three lowest frequency solid modes with pre-stress ($\hat{\boldsymbol{\Xi}}_{\mathrm{s}} \neq 0$). (b) Leading complex-conjugate eigenvalues as a function of the number N_s of solid vibration modes in the truncated modal basis. The time needed for the LU decomposition of the reduced matrices is indicated in the last column, as a percentage of the time needed to invert the full (i.e. without modal projection) matrix.

3.4. Results for the reduced eigenvalue-problem

Rather than solving the full eigenvalue problem (37), we consider here the resolution of the reduced eigenvalue problem (42) obtained after projection of the solid dynamics onto free-vibrations modes (see the steps described in Section 2.5). More specifically, we investigate how the number of free-vibrations modes influence the accuracy of the leading eigenvalue.

For our test-cases with elongated structures, the free-vibration mode with the lowest frequency is a flexion mode with one vibration node at the clamped end, as represented on top in Fig. 11a. Then as the frequency increases, the number of vibration nodes in the corresponding mode increases as well (see Fig. 11a modes 2 and 3). For higher frequencies, compression modes also appear. Note that taking into account the initial steady strains has a significant influence on the computed frequencies: while the four first *in-vacuo* circular frequencies are 0.130, 0.842, 2.227 and 4.458, due to the presence of the pre-strains that tends to elongate the solid, the vibration frequencies are higher when the steady deformation $\hat{\boldsymbol{\Xi}}_{\mathrm{s}} \neq 0$ is taken into account for computing the uncoupled solid vibration frequencies. Namely, the four first pre-stressed frequencies are 0.602, 1.577, 3.421 and 5.579. In all what follows, the free vibration basis is therefore computed by taking into account these pre-stresses. Also note that the free vibration frequencies without initial strains that we have computed are in good agreement with those obtained in [30] (respectively 0.820, 2.287 and 4.498 for the second, third and fourth *in-vacuuo* circular frequencies, re-normalized according to the reference scales used in this paper).

The results obtained with mesh M_3 are reported in Fig. 11b. For $N_s = 5$, the basis for the flutter-induced case is constituted of five modes, the first one with $\omega_{s,1} = 0.602$ and the last one with $\omega_{s,5} = 8.584$. As the number of modes in the free vibration basis is increased, the leading eigenvalue of the approximate eigenvalue problem becomes closer to the leading eigenvalue of the full problem (reported in the last row). One notices that the approximate results become fairly good from $N_s = 5$. This makes sense, since the mode obtained with the full solver seems to be a combination of the bending modes 1, 2 and 3 (see for instance the solid displacement extracted from a cut $y = 0$ on Fig. 8c). Note that fewer modes are required to reconstruct correctly the frequency than to reconstruct the growth-rate. For $N_s = 5$, the deviation compared to the eigenvalue obtained with the full problem is of about 23% for the growth-rate and less than 2% for the frequency. In all cases the interest of the modal decomposition in terms of computing performance is clear. Even when a solid basis of 20 modes is considered, a speedup of at least about $4\times$ is observed for the LU factorization of the shifted system matrix (using a direct LU solver like MUMPS). The gain in terms of memory depends on the initial extension box size.

3.5. Bending and vibration of a three-dimensional flexible plate in a uniform cross-flow

The last test-case is a three-dimensional flexible plate facing a uniform incoming flow of velocity U_∞. The stability of the three-dimensional flow around the *rigid* plate was previously investigated by Marquet et Larsson [31]. Following them, we define the Reynolds number as $\mathcal{R}_\mathrm{e} = U_\infty h^*/\nu$ where the height of the plate h^* is used to non-dimensionalize all lengths. The non-dimensional thickness of the plate being fixed to 0.04, they varied the non-dimensional spanwise length L in the range $1 \leq L \leq 6$ and determined the critical Reynolds number for various eigenmodes. These unstable eigenmodes break one of the reflectional symmetries with respect to the planes $y = 0$ and $z = 0$ that are satisfied by the steady flow. Here, we focus on the longest plate $L = 6$ and set the Reynolds number to $\mathcal{R}_\mathrm{e} = 60$. For this value an unsteady eigenmode breaking the reflectional symmetry with respect to the plane $y = 0$ is unstable. Such eigenmode leads to the shedding of vortices whose axis is aligned with the z direction. Here, we consider that the flexible plate is clamped along its axis Oy and investigate the effect of the flexibility on the unsteady properties of the wake flow. As the stiffness is reduced, the plate bends in the streamwise direction as a result of the load exerted by the incoming flow. After computing the steady flow balancing the deformation of the plate for various stiffness, we determine its stability by computing the largest eigenmodes.

The plate is made of an elastic material characterized by a fixed Poisson coefficient $\nu_\mathrm{s} = 0.35$ and a non-dimensional Young modulus varying in the range $5 \times 10^5 \leq \mathcal{E}_s \leq 1 \times 10^{10}$. The fluid-to-solid density ratio is set to $\mathcal{M}_\mathrm{s} = 1$. The computational domain, sketched in Fig. 12, is a quarter of the physical domain, taking advantage of the reflectional symmetries, specified hereinafter, to reduce the computational cost. Dirichlet conditions are applied to the velocities at the inlet ($x = -10$), a stress-free boundary condition is applied at the outlet ($x = 20$) and slip boundary conditions are applied on the lateral planes ($z = 10$ and $y = 7$). The boundary conditions applied along the symmetry planes ($y = 0$ and $z = 0$) depend on the type of computations. The steady flow velocity and solid displacement fields exhibit the following reflectional symmetries

$$(\mathcal{S}_y) : \left(U, V, W, \Xi_s^x, \Xi_s^y, \Xi_s^z\right)(x, -y, z) = \left(U, -V, W, \Xi_s^x, -\Xi_s^y, \Xi_s^z\right)(x, y, z)$$
$$(\mathcal{S}_z) : \left(U, V, W, \Xi_s^x, \Xi_s^y, \Xi_s^z\right)(x, y, -z) = \left(U, V, -W, \Xi_s^x, \Xi_s^y, -\Xi_s^z\right)(x, y, z)$$

where (U, V, W) are the components of the steady flow velocity and $(\Xi_s^x, \Xi_s^y, \Xi_s^z)$ are the components of the steady solid displacement. For the steady-state computations, the following boundary conditions are thus applied on the symmetry planes

$$\left(\partial_y U, V, \partial_y W, \partial_y \Xi_s^x, \Xi_s^y, \partial_y \Xi_s^z\right)(x, 0, z) = \left(0, 0, 0, 0, 0, 0\right)$$
$$\left(\partial_z U, \partial_z V, W, \partial_z \Xi_s^x, \partial_z \Xi_s^y, \Xi_s^z\right)(x, y, 0) = \left(0, 0, 0, 0, 0, 0\right).$$

The eigenmode of interest satisfies the symmetry $(\mathcal{S}_z)$ but breaks the symmetry $(\mathcal{S}_y)$. For the eigenvalue computations, the following boundary conditions are therefore applied on the symmetry planes

$$\left(u^\circ, \partial_y v^\circ, w^\circ, \xi_s^\circ, \partial_y \psi_s^\circ, \eta_s^\circ\right)(x, 0, z) = \left(0, 0, 0, 0, 0, 0\right)$$
$$\left(\partial_z u^\circ, \partial_z v^\circ, w^\circ, \partial_z \xi_s^\circ, \partial_z \psi_s^\circ, \eta_s^\circ\right)(x, y, 0) = \left(0, 0, 0, 0, 0, 0\right)$$

where $(\xi_s^\circ, \psi_s^\circ, \eta_s^\circ)$ are the solid components of an eigenmode. More details about the various combination of symmetries satisfied by the eigenmodes can be found in [31]. The computations are performed using a mesh made of 566 216 tetrahedra that yields to 3 751 070 degrees of freedom for the steady-state problem and 3 905 378 for the eigenvalue problem. For both the steady computations and eigenvalue problems investigated here, the block Gauss–Seidel preconditioner requires on the order of ten iterations to converge. Combined with direct LU decompositions for each sub-block, this provides relatively fast and robust computations for moderately large 3d problems. To compute large steady deformations of the plate achieved when the stiffness $\mathcal{E}_s$ is reduced, an updated Lagrangian approach [42] is used together with a continuation on the Young modulus, so as to deform progressively the computational domain.

The steady-state solutions are described in Fig. 13. Contours of the flow velocity magnitude (blue) in the plane $y = 0$ and the pressure at the surface of the plate (orange) computed for $\mathcal{E}_s = 5 \times 10^5$ are shown. The pressure is maximum in the centre of the plate, then decreases as one moves towards the edges thanks to the streamlining effect induced by the deformation of the plate. For the above value of the stiffness, the displacement of the plate in the streamwise direction is of the same order of magnitude as the height of the plate. The shape of the back-flow region in the wake of the plate is modified by the bending of the plate, as emphasized by the translucent grey

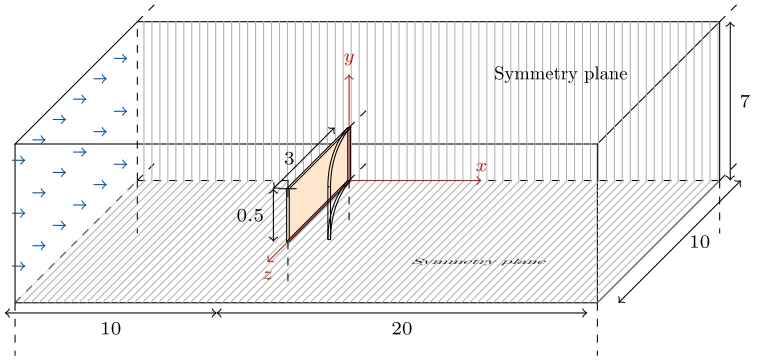

Fig. 12. Computational domain of the three-dimensional flexible plate (orange) immersed in an incoming uniform flow sketched with blue arrows. The plate is of (non-dimensional) height 1, length 6 and thickness 0.04. Only a quarter of the physical domain is used for the computation, exploiting the reflectional symmetries of the problem. The boundary conditions applied on the symmetry planes are specified in the text. A probe point P is placed in the free corner of the plate at position $(0, 0.5, 3)$ marked with a $+$ symbol. (For interpretation of the references to colour in this figure legend, the reader is referred to the web version of this article.)

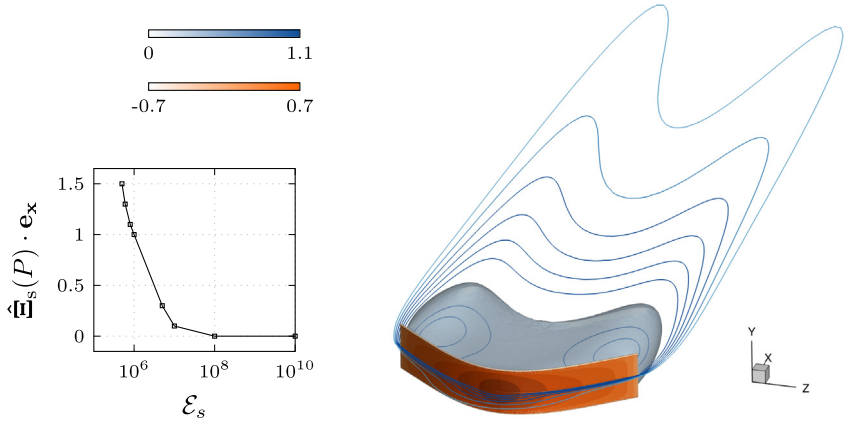

Fig. 13. Steady fluid–structure equilibrium for the three-dimensional flexible plate facing an incoming uniform flow. The pictures on the right-hand side display top and side views of the steady solution obtained for $\mathcal{E}_s = 5 \times 10^5$ in the symmetry planes $y = 0$ (top) and $z = 0$ (bottom). Velocity magnitude contours in the $y = 0$ plane are depicted with the blue colour, and the pressure at the surface of the plate is depicted with the orange colour. The back-flow region in the wake of the plate is delimited with the grey translucent surface for which the streamwise velocity is -0.05. The left-hand side picture represents the streamwise displacement ξ_s^b of the point P as a function of the stiffness $\mathcal{E}_s$.

interface that delimits the back-flow region. The larger back-flow velocities are obtained near the tip of the plate. The streamwise displacement of the tip (point P shown in Fig. 12) is reported in the left-hand side picture as a function of the stiffness. Small displacements of the plate are obtained down to $\mathcal{E}_s = 10^7$. Further decreasing the stiffness yields to a linear increase of the displacement up to 1, the (non-dimensional) height of the plate.

The largest eigenvalues are computed for a stiff ($\mathcal{E}_s = 1 \times 10^{10}$) and a flexible ($\mathcal{E}_s = 5 \times 10^5$) plate. The eigenvalue spectra are reported in Fig. 14a with symbols $\square$ and $\times$, respectively. The unstable pair of eigenvalues obtained for the stiff plate compares well with results given in Fig. 5 in [31] where an angular frequency of 0.529 is reported for the unstable mode. In the case where $\mathcal{E}_s = 1 \times 10^{10}$, an angular frequency of 0.518 is found (deviation of about 2 %). Considering now the flexible plate, one clearly sees that the pair of complex eigenvalues is stabilized and its frequency is increased ($2.4 \times 10^{-3} \pm 0.80\,\mathbf{i}$). The vibrating motion given by the solid component of the eigenmode that corresponds to the leading pair of eigenvalues is shown in Fig. 14b for the flexible plate. Four snapshots in the period of oscillation are depicted. The displacement is a combination of torsional motion about the z axis and a smaller-amplitude up-and-down flexion along the y axis. As shown in Figs. 14c–14e, the flow velocity components exhibit an oscillating pattern in the streamwise direction, typical of the vortex-shedding pattern also

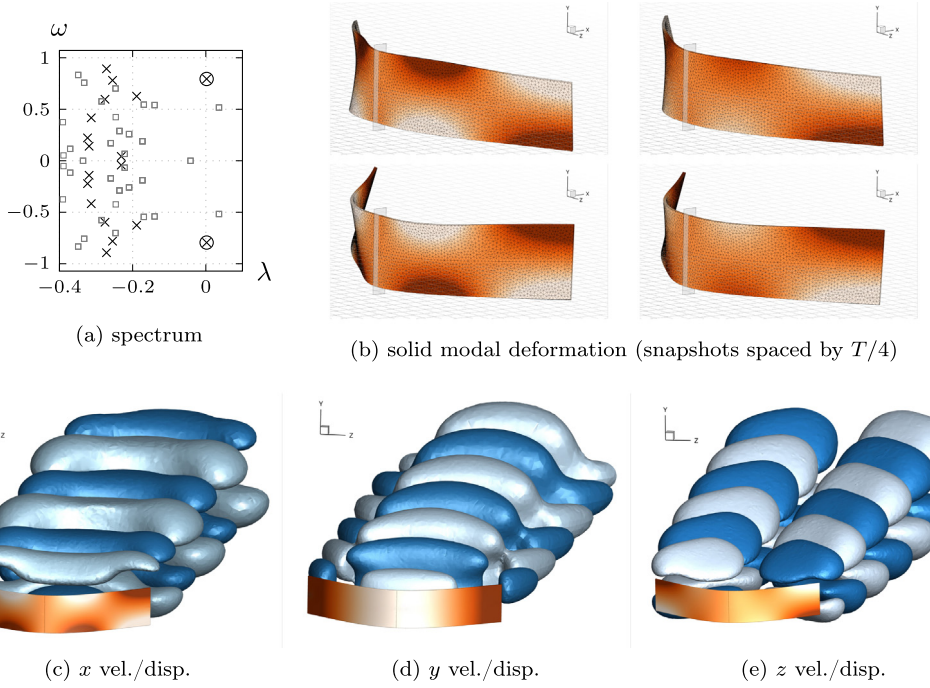

(a) spectrum

(b) solid modal deformation (snapshots spaced by $T/4$)

(c) x vel./disp.

(d) y vel./disp.

(e) z vel./disp.

Fig. 14. Linear stability analysis of steady solutions computed for flexible plates of various stiffness $\mathcal{E}_s$. (a) Eigenvalue spectra for a stiff plate (□, $\mathcal{E}_s = 10^{10}$) and a flexible plate (×, $\mathcal{E}_s = 5 \times 10^5$) where the unstable eigenvalue is circled. (b) Three-dimensional view of the instantaneous deformation of the flexible plate induced by the solid component of the eigenmode associated to the pair of marginal complex eigenvalues (×). Snapshots are displayed (in the clockwise direction) at times 1/4, 1/2, 3/4 and 1 of the oscillation period $T = 2\pi/\omega$, ω being the imaginary part of the eigenvalue. The colours indicate the deformation magnitude. The rectangle placed in the plane $z = 0$ materializes the clamped position of the plate. (c,d,e) Plots of the x, y and z components of the flow velocity (blue) and solid displacement (orange) of the real part of the unstable eigenmode. For the fluid, iso-contours are shown for a positive (light blue) and a negative (dark blue) value. (For interpretation of the references to colour in this figure legend, the reader is referred to the web version of this article.)

observed for the rigid plate (see [31]). The spatial structure is mainly modified by the streamlining effect induced by the bending of the plate. For instance, the transverse size of the region where the largest y velocity perturbations occur is reduced.

This three-dimensional test-case shows that the present approach allows to compute steady fluid–solid configurations for which the solid is strongly deformed by the fluid loads and to determine the three-dimensional fluid and solid modal perturbations that are responsible for the destabilization of this steady state.

Conclusion

Inspired by previous numerical studies aiming at designing fully implicit fluid–structure solvers, we proposed an approach for performing linear stability analyses of strongly coupled fluid–structure interaction problems in the ALE framework. This approach is based on an exact linearization of the continuous ALE fluid–structure equations formulated for the Lagrangian-based perturbation in the steady deformed configuration. Using a standard finite-element method for the spatial discretization of the eigenvalue problem, the linear stability analysis has been performed for two bi-dimensional configurations exhibiting distinct physical fluid–structure interaction mechanisms (the vortex-induced vibrations of an elastic plate attached to a cylinder, and the flutter instability of a flag in a channel flow), and a three-dimensional case involving large static displacements. The proposed approach is found to be numerically consistent, and gives accurate predictions of instability thresholds at a very moderate cost compared to non-linear simulations.

As mentioned before, our formulation is closely related to non-linear ALE codes, and thus its development can also be very easily re-used for this purpose. On a broader perspective, it can also be adapted at low costs for computing adjoint eigensolutions for parameter estimation or optimal control problems. On the other hand, we plan

to compare this approach to Eulerian-based methods, and investigate in particular the numerical behaviour induced by the presence of the non-standard added-stiffness terms.

Direct solvers are particularly efficient in eigenvalues problems, that require multiple matrix inversions. In the case of large-scale 3d problems however, even a fully distributed LU decomposition becomes prohibitive in terms of memory, and it is thus mandatory to adopt an iterative method. The development of efficient preconditioners for handling the inversion of the fluid subproblem that appears in the block Gauss–Seidel loop evoked in section Section 2.5 would therefore be beneficial to address this limitation.

Acknowledgement

This project has received funding from the European Research Council (ERC) under the European Union's Horizon 2020 research and innovation program (Grant Agreement No. 638307).

Appendix A. Linearized operators

The linearized operator that appear in the weak formulation in Section 2.3 writes as follows, with $\boldsymbol{q}_{\mathrm{f}}^{\circ} = (\boldsymbol{u}^{\circ}, p^{\circ}, \boldsymbol{\lambda}^{\circ})$, $\boldsymbol{q}_{\mathrm{e}}^{\circ} = \left(\boldsymbol{\xi}_{\mathrm{e}}^{\circ}, \boldsymbol{\lambda}_{\mathrm{e}}^{\circ}\right)$, $\boldsymbol{q}_{\mathrm{s}}^{\circ} = (\boldsymbol{\xi}_{\mathrm{s}}^{\circ}, \boldsymbol{u}_{\mathrm{s}}^{\circ})$, $\boldsymbol{\psi}_{\mathrm{f}} = (\boldsymbol{\psi}^{\boldsymbol{u}}, \psi^{p}, \boldsymbol{\psi}^{\boldsymbol{\lambda}})$, $\boldsymbol{\psi}_{\mathrm{s}} = (\boldsymbol{\psi}_{\mathrm{s}}^{\boldsymbol{\xi}}, \boldsymbol{\psi}_{\mathrm{s}}^{\boldsymbol{u}})$ and $\boldsymbol{\psi}_{\mathrm{e}} = (\boldsymbol{\psi}_{\mathrm{e}}^{\boldsymbol{\xi}}, \boldsymbol{\psi}_{\mathrm{e}}^{\boldsymbol{\lambda}})$. The fluid operators are

$$
\begin{aligned}
\mathcal{B}_{\mathrm{f}}(\boldsymbol{\psi}_{\mathrm{f}}, \boldsymbol{q}_{\mathrm{f}}^{\circ}) &= \int_{\Omega_{\mathrm{f}}} \boldsymbol{u}^{\circ} \cdot \boldsymbol{\psi}^{\boldsymbol{u}} \,\mathrm{d}\Omega, \\
\mathcal{B}_{\mathrm{fe}}(\boldsymbol{\psi}_{\mathrm{f}}, \boldsymbol{q}_{\mathrm{e}}^{\circ}) &= -\int_{\Omega_{\mathrm{e}}} (\boldsymbol{\nabla U})\boldsymbol{\xi}_{\mathrm{e}}^{\circ} \cdot \boldsymbol{\psi}^{\boldsymbol{u}} \,\mathrm{d}\Omega, \\
\mathcal{A}_{\mathrm{f}}(\boldsymbol{\psi}_{\mathrm{f}}, \boldsymbol{q}_{\mathrm{f}}^{\circ}) &= -\int_{\Omega_{\mathrm{f}}} \left(\left((\boldsymbol{\nabla U})\boldsymbol{u}^{\circ} + (\boldsymbol{\nabla u}^{\circ})\boldsymbol{U} \right) \cdot \boldsymbol{\psi}^{\boldsymbol{u}} + \frac{2}{\mathcal{R}_{\mathrm{e}}} \mathbf{D}(\boldsymbol{u}^{\circ}) : \boldsymbol{\nabla \psi}^{\boldsymbol{u}} \right) \mathrm{d}\Omega \\
&\quad + \int_{\Omega_{\mathrm{f}}} \left(p^{\circ} \nabla \cdot \boldsymbol{\psi}^{\boldsymbol{u}} + \psi^{p} \nabla \cdot \boldsymbol{u}^{\circ} \right) \mathrm{d}\Omega + \int_{\Gamma} \left(\boldsymbol{\lambda}^{\circ} \cdot \boldsymbol{\psi}^{\boldsymbol{u}} + \boldsymbol{\psi}^{\boldsymbol{\lambda}} \cdot \boldsymbol{u}^{\circ} \right) \mathrm{d}\Gamma, \\
\mathcal{A}_{\mathrm{fe}}(\boldsymbol{\psi}_{\mathrm{f}}, \boldsymbol{q}_{\mathrm{e}}^{\circ}) &= -\int_{\Omega_{\mathrm{e}}} \left((\boldsymbol{\nabla U})\boldsymbol{\Phi}'(\boldsymbol{\xi}_{\mathrm{e}}^{\circ})\,\boldsymbol{U} \cdot \boldsymbol{\psi}^{\boldsymbol{u}} + \frac{2}{\mathcal{R}_{\mathrm{e}}} \mathbf{D}(\boldsymbol{U})\boldsymbol{\Phi}'(\boldsymbol{\xi}_{\mathrm{e}}^{\circ})^{\mathrm{T}} : \boldsymbol{\nabla \psi}^{\boldsymbol{u}} \right) \mathrm{d}\Omega \\
&\quad + \frac{1}{\mathcal{R}_{\mathrm{e}}} \int_{\Omega_{\mathrm{e}}} \left(\boldsymbol{\nabla U} \boldsymbol{\nabla} \boldsymbol{\xi}_{\mathrm{e}}^{\circ} + \boldsymbol{\nabla} \boldsymbol{\xi}_{\mathrm{e}}^{\circ \mathrm{T}} \boldsymbol{\nabla U}^{\mathrm{T}} \right) : \boldsymbol{\nabla \psi}^{\boldsymbol{u}} \,\mathrm{d}\Omega \\
&\quad + \int_{\Omega_{\mathrm{e}}} \left(P\, \boldsymbol{\nabla \psi}^{\boldsymbol{u}} + \psi^{p}\, \boldsymbol{\nabla U} \right) : \boldsymbol{\Phi}'(\boldsymbol{\xi}_{\mathrm{e}}^{\circ})^{\mathrm{T}} \,\mathrm{d}\Omega, \\
\mathcal{A}_{\mathrm{fs}}(\boldsymbol{\psi}_{\mathrm{f}}, \boldsymbol{q}_{\mathrm{s}}^{\circ}) &= -\int_{\Gamma} \boldsymbol{\lambda}^{\circ} \cdot \boldsymbol{\psi}^{\boldsymbol{u}} \,\mathrm{d}\Gamma,
\end{aligned}
$$

where $\mathbf{D}(\boldsymbol{u}^{\circ}) = 1/2\,(\boldsymbol{\nabla u}^{\circ} + \boldsymbol{\nabla u}^{\circ \mathrm{T}})$, and where the Nanson's formula [38] has been used so as to rewrite the fluid continuity equation as $\boldsymbol{\nabla} \cdot (\boldsymbol{\Phi}(\boldsymbol{\xi}')\,\boldsymbol{U}) = \boldsymbol{\Phi}(\boldsymbol{\xi}')^{\mathrm{T}} : \boldsymbol{\nabla U} = 0$, which lowers the differentiation order on $\boldsymbol{\xi}'$. The solid operators are

$$
\begin{aligned}
\mathcal{B}_{\mathrm{s}}(\boldsymbol{\psi}_{\mathrm{s}}, \boldsymbol{q}_{\mathrm{s}}^{\circ}) &= \int_{\Omega_{\mathrm{s}}} \left(\frac{\mathcal{M}_{\mathrm{s}}}{\hat{\mathrm{J}}(\hat{\boldsymbol{\Xi}}_{\mathrm{s}})} \boldsymbol{u}_{\mathrm{s}}^{\circ} \cdot \boldsymbol{\psi}_{\mathrm{s}}^{\boldsymbol{u}} + \boldsymbol{\xi}_{\mathrm{s}}^{\circ} \cdot \boldsymbol{\psi}_{\mathrm{s}}^{\boldsymbol{\xi}} \right) \mathrm{d}\Omega, \\
\mathcal{A}_{\mathrm{s}}(\boldsymbol{\psi}_{\mathrm{s}}, \boldsymbol{q}_{\mathrm{s}}^{\circ}) &= \int_{\Omega_{\mathrm{s}}} \left(\boldsymbol{u}_{\mathrm{s}}^{\circ} \cdot \boldsymbol{\psi}_{\mathrm{s}}^{\boldsymbol{\xi}} - \mathbf{P}'(\boldsymbol{\xi}_{\mathrm{s}}^{\circ}; \hat{\boldsymbol{\Xi}}_{\mathrm{s}}) : \boldsymbol{\nabla} \boldsymbol{\psi}_{\mathrm{s}}^{\boldsymbol{u}} \right) \mathrm{d}\Omega.
\end{aligned}
$$

The extension operators (with a Laplace extension equation) write as

$$
\begin{aligned}
\mathcal{A}_{\mathrm{e}}(\boldsymbol{\psi}_{\mathrm{e}}, \boldsymbol{q}_{\mathrm{e}}^{\circ}) &= -\int_{\Omega_{\mathrm{e}}} \boldsymbol{\nabla} \boldsymbol{\xi}_{\mathrm{e}}^{\circ} : \boldsymbol{\nabla} \boldsymbol{\psi}_{\mathrm{e}}^{\boldsymbol{\xi}} \,\mathrm{d}\Omega + \int_{\Gamma} \left(\boldsymbol{\lambda}_{\mathrm{e}}^{\circ} \cdot \boldsymbol{\psi}_{\mathrm{e}}^{\boldsymbol{\xi}} + \boldsymbol{\psi}_{\mathrm{e}}^{\boldsymbol{\lambda}} \cdot \boldsymbol{\xi}_{\mathrm{e}}^{\circ} \right) \mathrm{d}\Gamma, \\
\mathcal{A}_{\mathrm{es}}(\boldsymbol{\psi}_{\mathrm{e}}, \boldsymbol{q}_{\mathrm{s}}^{\circ}) &= -\int_{\Gamma} \boldsymbol{\xi}_{\mathrm{s}}^{\circ} \cdot \boldsymbol{\psi}_{\mathrm{e}}^{\boldsymbol{\lambda}} \,\mathrm{d}\Gamma.
\end{aligned}
$$

Table B.4
(a) Characteristics of meshes used for the vortex-induced vibration test-case and the validation cases, number of triangles N_t and the maximum (resp. minimum) triangle size $\Delta^{\max}$ (resp. $\Delta^{\min}$) for various meshes. (b) For the case FSI1, lift and drag coefficients $\mathcal{C}_{\mathrm{D}}$ and $\mathcal{C}_{\mathrm{L}}$ for the cylinder and the plate, and displacement $\hat{\boldsymbol{\Xi}}_{\mathrm{s}} = (\xi_B^b, \psi_B^b)$ at point $B(3.99, 0)$.

(a) Mesh characteristics

	N_t	$\Delta^{\max}$	$\Delta^{\min}$
T_0	3 298	0.71	0.113
T_1	8 922	0.32	0.051
T_2	16 176	0.26	0.030
T_3	34 958	0.22	0.018
T_4	64 828	0.15	0.012
T_5	120 978	0.10	0.009

(b) Case FSI1

	$\mathcal{C}_{\mathrm{D}}$	$\mathcal{C}_{\mathrm{L}}$	$\xi_B^b \cdot 10^{-4}$	$\psi_B^b \cdot 10^{-3}$
T_0	7.092	0.400	2.304	5.129
T_1	7.127	0.381	2.233	8.287
T_2	7.131	0.382	2.232	8.073
T_3	7.132	0.385	2.182	7.910
T_4	7.135	0.383	2.155	7.816
T_5	7.134	0.382	2.064	7.476
[29]	7.147	0.382	2.270	8.209

Table B.5
FSI3 benchmark, mesh convergence: values of the mean solid x and y displacements $\bar{\xi}(B)$ and $\bar{\psi}(B)$, solid x and y displacement amplitude $\delta\xi(B)$ and $\delta\psi(B)$ at point $B(3.99, 0)$, and mean aerodynamic drag and lift coefficients $\overline{\mathcal{C}_{\mathrm{D}}}$ and $\overline{\mathcal{C}_{\mathrm{L}}}$.

	$\bar{\xi}(B)$	$\delta\xi(B)$	$\bar{\psi}(B)$	$\delta\psi(B)$	$\overline{\mathcal{C}_{\mathrm{D}}}$	$\overline{\mathcal{C}_{\mathrm{L}}}$
T0	Blow-up	Blow-up	Blow-up	Blow-up	Blow-up	Blow-up
T1	−0.029	0.028	0.014	0.349	2.274	0.009
T2	−0.029	0.027	0.014	0.348	2.298	0.013
T3	−0.028	0.027	0.014	0.342	2.302	0.012
[29]	−0.027	0.025	0.015	0.344	2.286	0.011

Appendix B. Validation of the steady and unsteady non-linear solvers

A non-linear solver is required to compute steady solutions. In order to validate the stability analysis, we also came to compute time-dependent solutions. We have chosen to use a solver which is very similar to those described for instance in [27,51], and is able to compute both unsteady and steady strongly coupled fluid–structure solutions. The non-linear system is written in the reference configuration $\hat{\Omega}$. A fully implicit scheme is derived, and each time-step is solved by a Newton loop in which the Jacobian matrix is reassembled only if the residuals increase from iteration to iteration. This solver is also implemented using FreeFem++. Time-dependent solutions are computed with a second-order shifted Crank–Nicholson scheme and a small time-step $\Delta t = 0.01$ — shifting the Crank–Nicholson scheme with Δt provides a gain in numerical stability [51], while steady solutions are obtained by using an implicit Euler scheme associated with a large time-step. Typically, taking $\Delta t = 10^{12}$ is then the same as solving the steady problem, and results in a converged solution in one single non-linear Newton step provided that the initial guess is good enough. Taking smaller time steps like $\Delta t \simeq 1$ results in a convergence towards the steady solution in a few time-steps, while too small time-steps result in an unsteady solution in the case where the physical problem is indeed time-dependent. Unlike the perturbation problems where the extension displacement is by definition infinitesimal, large finite-amplitude displacement of the fluid mesh might occur. The extension operator $\hat{\boldsymbol{\Sigma}}_{\mathrm{e}}$ is then chosen carefully so as to allow large deformation of the fluid mesh. As done in [35,36], the extension operator has been defined as a diffusion operator with space-varying coefficients in order to stiffen the elements close to the fluid–solid boundary. The extension domain is chosen large enough so that it allows possibly large deformations.

A set of various meshes are used to test the algorithms, named T_0 to T_5 from the coarsest to the finest. In Table B.4a, the number of triangles in the domain is reported, as well as the minimal edge length in the mesh. The steady solver is validated on the case FSI1 from [29], for which the parameters are $\mathcal{R}_{\mathrm{e}} = 20$, $E_s = 35000$, $\nu_s = 0.4$ and $\mathcal{M}_{\mathrm{s}} = 1$. The time-dependent solver is validated on the case FSI3, where $\mathcal{R}_{\mathrm{e}} = 200$, $E_s = 1400$, $\nu_s = 0.4$ and $\mathcal{M}_{\mathrm{s}} = 1$.

As seen in Table B.4b, our steady solutions are in good agreement with the reference values of case FSI1 given in [29]. Our results are also within the margins obtained in the paper that summarizes the computations

of various groups [52]. The same observation holds for the unsteady case FSI3, as seen in Table B.5, where the mean and amplitude of the plate displacement at point $B(3.99, 0)$ are reported, as well as the mean aerodynamic coefficients. We used the conventions from [29] to compute the mean value as $1/2(\max+\min)$ and the amplitude as $1/2(\max-\min)$. A time-step convergence study has also been performed on mesh T_1, where we varied Δt between 0.2 and 0.005. A convergence up to the two first digits is observed from $\Delta t = 0.01$.

References

[1] R.L. Bisplinghoff, H. Ashley, R.L. Halfman, Aeroelasticity, Addison-Wesley Publishing Company, 1955.
[2] E.H. Dowell, R. Clark, D. Cox, et al., A Modern Course in Aeroelasticity, Vol. 3, Springer, 2004.
[3] E. de Langre, Fluides et solides, Les Éditions de l'École polytechnique, 2002.
[4] T. Theodorsen, General Theory of Aerodynamic Instability and the Mechanism of Flutter, 1949.
[5] M. Lesoinne, M. Sarkis, U. Hetmaniuk, C. Farhat, A linearized method for the frequency analysis of three-dimensional fluid/structure interaction problems in all flow regimes, Comput. Methods Appl. Mech. Engrg. 190 (24) (2001) 3121–3146.
[6] E.H. Dowell, K.C. Hall, Modeling of fluid-structure interaction, Annu. Rev. Fluid Mech. 33 (1) (2001) 445–490.
[7] D. Sipp, O. Marquet, P. Meliga, A. Barbagallo, Dynamics and control of global instabilities in open-flows: a linearized approach, Appl. Mech. Rev. 63 (3) (2010) 030801.
[8] V. Theofilis, Global linear instability, Annu. Rev. Fluid Mech. 43 (2011) 319–352.
[9] M. Lighthill, On displacement thickness, J. Fluid Mech. 4 (04) (1958) 383–392.
[10] P. Raj, B. Harris, Using surface transpiration with an Euler method for cost-effective aerodynamic analysis, in: 1993 AIAA 11 th Applied Aerodynamics Conference, 1993.
[11] G. Mortchelewicz, Application of the linearized euler equations to flutter, in: Office National d'Etudes et de Recherches Aérospatiales (ONERA), Information scientifique et technique et publications, 1997.
[12] C. Fisher, A. Arena, On the transpiration method for efficient aeroelastic analysis using an Euler solver, AIAA Paper (1996) 96–3436.
[13] N. Bekka, M. Sellam, A. Chpoun, Aeroelastic stability analysis of a flexible over-expanded rocket nozzle using numerical coupling by the method of transpiration, J. Fluids Struct. 56 (2015) 89–106.
[14] G. Allaire, M. Schoenauer, Conception Optimale de Structures, Vol. 58, Springer, 2007.
[15] J. Sokolowski, J.-P. Zolesio, Introduction to shape optimization, in: Introduction to Shape Optimization, Springer, 1992.
[16] T. Richter, Goal-oriented error estimation for fluid-structure interaction problems, Comput. Methods Appl. Mech. Engrg. 223 (2012) 28–42.
[17] T. Richter, T. Wick, Optimal control and parameter estimation for stationary fluid-structure interaction problems, SIAM J. Sci. Comput. 35 (5) (2013) B1085–B1104.
[18] K. Van der Zee, E. Van Brummelen, I. Akkerman, R. De Borst, Goal-oriented error estimation and adaptivity for fluid–structure interaction using exact linearized adjoints, Comput. Methods Appl. Mech. Engrg. 200 (37) (2011) 2738–2757.
[19] M.Á. Fernandez, P. Le Tallec, Linear stability analysis in fluid-structure interaction with transpiration. part i: Formulation and mathematical analysis, Comput. Methods Appl. Mech. Engrg. 192 (2003) 4805–4835.
[20] M.Á. Fernandez, P. Le Tallec, Linear stability analysis in fluid-structure interaction with transpiration. part ii: Numerical analysis and applications, Comput. Methods Appl. Mech. Engrg. 192 (2003) 4837–4873.
[21] T. Hughes, W. Liu, T. Zimmermann, Lagrangian-Eulerian finite element formulation for incompressible viscous flows, Comput. Methods Appl. Mech. Engrg. 29 (1981) 329–349.
[22] M. Lesoinne, C. Farhat, Stability analysis of dynamic meshes for transient aeroelastic computations, in: 11th Computational Fluid Dynamics Conference, 1993, p. 3325.
[23] F. Nobile, Numerical Approximation of Fluid-Structure Interaction Problems with Application to Haemodynamics (Ph.D. thesis), EPFL, 2001.
[24] P. Causin, J.-F. Gerbeau, F. Nobile, Added-mass effect in the design of partitioned algorithms for fluid-structure problems, Comput. Methods Appl. Mech. Engrg. 194 (42) (2005) 4506–4527.
[25] M.Á. Fernandez, M. Moubachir, A newton method using exact jacobians for solving fluid-structure coupling, Comput. Struct. 83 (2) (2005) 127–142.
[26] J. Hron, S. Turek, A monolithic fem/multigrid solver for an ALE formulation of fluid-structure interaction with applications in biomechanics, in: Fluid-Structure Interaction, Springer, 2006, pp. 146–170.
[27] T. Wick, Solving monolithic fluid-structure interaction problems in Arbitrary Lagrangian Eulerian coordinates with the deal. ii library, Arch. Numer. Softw. 1 (1) (2013) 1–19.
[28] T. Richter, A monolithic geometric multigrid solver for fluid-structure interactions in ale formulation, Internat. J. Numer. Methods Engrg. 104 (5) (2015) 372–390.
[29] S. Turek, J. Hron, Proposal for numerical benchmarking of fluid-structure Interaction between an elastic object and laminar Incompressible flow, Springer, 2006.
[30] J. Cisonni, A.D. Lucey, N.S. Elliott, M. Heil, The stability of a flexible cantilever in viscous channel flow, J. Sound Vib. 396 (2017) 186–202.
[31] O. Marquet, M. Larsson, Global wake instabilities of low aspect-ratio flat-plates, Eur. J. Mech. B Fluids 49 (2015) 400–412.
[32] T. Leclercq, E. de Langre, Vortex-induced vibrations of cylinders bent by the flow, J. Fluids Struct. 80 (2018) 77–93.
[33] R.W. Ogden, Non-Linear Elastic Deformations, Dover, 1997.

[34] J. Donea, A. Huerta, J.-P. Ponthot, A. Rodrigez-Ferran, Arbitrary Lagrangian-Eulerian methods, Encyclopedia Comput. Mech. (2004) URL http://dx.doi.org/10.1002/0470091355.ecm009.
[35] K. Stein, T. Tezduyar, R. Benney, Mesh moving techniques for fluid-structure interactions with large displacements, ASME J. Appl. Mech. 70 (2003) 58–63.
[36] T. Wick, Fluid-structure interactions using different mesh motion techniques, Comput. Struct. 89 (13) (2011) 1456–1467.
[37] B.T. Helenbrook, Mesh deformation using the biharmonic operator, Internat. J. Numer. Methods Engrg. 56 (7) (2003) 1007–1021.
[38] R. Aris, Vectors, Tensors and the Basic Equations of Fluid Mechanics, Courier Corporation, 2012.
[39] P. Le Tallec, J. Mouro, Fluid structure interaction with large structural displacements, Comput. Methods Appl. Mech. Engrg. (2001).
[40] T. Richter, Fluid-Structure Interactions: models, Analysis and Finite Elements, Vol. 118, Springer, 2017.
[41] O. Ghattas, X. Li, A variational finite element method for stationary nonlinear fluid-solid interaction, J. Comput. Phys. 121 (2) (1995) 347–356.
[42] S. Etienne, D. Pelletier, An updated Lagrangian monolithic formulation for steady-state fluid-structure interaction problems, in: 43 rd AIAA Aerospace Sciences Meeting and Exhibit, 2005, p. 2005.
[43] S. Deparis, D. Forti, G. Grandperrin, A. Quarteroni, Facsi: A block parallel preconditioner for fluid–structure interaction in hemodynamics, J. Comput. Phys. 327 (2016) 700–718.
[44] I. Babuška, The finite element method with Lagrangian multipliers, Numer. Math. 20 (3) (1973) 179–192.
[45] T. Richter, T. Wick, Finite elements for fluid-structure interaction in ALE and fully Eulerian coordinates, Comput. Methods Appl. Mech. Engrg. 199 (41) (2010) 2633–2642.
[46] V. Girault, P. Raviart, Finite Element Methods for Navier-Stokes Equations, in: Springer Series in Computational Mathematics, Springer, 1985.
[47] F. Hecht, New development in freefem++, J. Numer. Math. 20 (3–4) (2012) 251–265.
[48] R. Lehoucq, D. Sorensen, C. Yang, ARPACK Users' Guide: Solution of Large Scale Eigenvalue Problems with Implicitly Restarted Arnoldi Methods, 1997, URL http://www.caam.rice.edu/software/ARPACK/.
[49] P. Amestoy, A. Buttari, A. Guermouche, J.-Y. L'Excellent, B. Ucar, Mumps: A Multifrontal Massively Parallel Sparse Direct Solver, 2013, URL http://mumps.enseeiht.fr.
[50] S. Mittal, Lock-in in vortex-induced vibration, J. Fluid Mech. 794 (2016) 565–594.
[51] T. Richter, T. Wick, On time discretizations of fluid-structure interactions, in: Multiple Shooting and Time Domain Decomposition Methods, Springer, 2015, pp. 377–400.
[52] S. Turek, J. Hron, M. Razzaq, H. Wobker, M. Schäfer, Numerical benchmarking of fluid-structure interaction: A comparison of different discretization and solution approaches, in: Fluid Structure Interaction II, Springer, 2011, pp. 413–424.